
ALMA MATER STUDIORUM - UNIVERSITÀ DI BOLOGNA
DEPARTMENT OF STATISTICAL SCIENCES

**Second Cycle Degree
in
Quantitative Finance**

**Rough Fractional Stochastic Volatility:
A Tale of Two Measures**

DEFENDED BY

Mengoni Gabriele

Student ID: 0001123008

SUPERVISOR

Professor

Lanconelli Alberto

December Graduation Session

Academic Year 2024 - 2025

Abstract

In this study we explore the mathematical foundation, the calibration, and we assess the performance of the Rough Fractional Stochastic Volatility (RFSV) model, which is a variation made by Gatheral, of the Fractional Stochastic Volatility (FSV) process, originally proposed by Comte and Renault in 1998. The difference between the two concepts lies in the value given to the Hurst exponent (H); in the former it is assumed to be smaller than $1/2$, by contrast, in the latter it is higher than that. We propose a two-measure calibration where the Hurst parameter is assumed to be a structural property of the underlying process therefore it is estimated statistically under the \mathbb{P} measure, as in Gatheral. The other parameters are then found with respect to the \mathbb{Q} measure, in order to obtain a set of coefficients able to price derivatives under the risk-neutral setting. We then assess the goodness of the fit by various metrics and by comparing it with the classic Heston model, the standard for stochastic volatility. In the final part we give a small application of our model by pricing two path-dependent exotic options.

Acknowledgements.

To all who have been part of this journey.

To the pursuit of greater things.

To what the future holds.

Ad maiora.

Contents

1 Fractional Brownian Motion.	8
1.1 Fractional Brownian Motion.	9
1.2 Properties of fBM.	10
1.3 Construction of fBM.	11
2 The models.	13
2.1 Theoretical setting.	13
2.1.1 Ornstein-Uhlenbeck.	14
2.1.2 Fractional Ornstein-Uhlenbeck.	15
2.2 The Fractional Stochastic Volatility Model.	15
2.2.1 The Long-Memory process.	16
2.2.2 Statistical properties of σ_t in the FSV model.	17
2.2.3 Discretization of the model.	17
2.2.4 The Global Filtering Model.	18
2.2.5 Integration scheme.	19
2.3 The Heston model.	20
2.3.1 The Heston equation.	20
3 Statistical Description and Volatility Surface Smoothing.	21
3.1 Data Description.	21
3.1.1 Price series.	21
3.1.2 Options chain.	22
3.2 Objective function: fitting the SVI.	23
3.2.1 The raw SVI parametrization.	23
3.2.2 Checking the RND.	24
4 Estimation Methods.	26
4.1 Realized Volatility Estimation.	26
4.1.1 Model with uncertainty zones.	26
4.1.2 Estimation procedure.	27
4.2 Parameters estimation.	29
4.2.1 \mathbb{P} vs \mathbb{Q}	29
4.2.2 H estimation.	29
4.2.3 Sanity check of the method.	31
4.3 Other parameters.	31
4.3.1 Differential Evolution algorithm.	32
4.3.2 Loss and Objective functions.	33
4.4 Computational aspects.	34
4.4.1 RFSV.	34
4.4.2 Heston.	35

4.5 Calibration routine.	36
5 Results.	37
5.1 Evaluation metric.	38
5.2 Short-term fit.	39
5.3 Medium-term fit.	41
5.4 Out of sample fit.	42
5.5 Surmise.	44
5.6 Application.	44
5.6.1 The Asian option.	45
5.6.2 The Lookback option.	45
5.6.3 Pricing.	46
6 Conclusion.	47
7 Appendix A.	48
7.1 Proof of (1).	48
7.2 Proof of (4)	48
7.3 Proof of (inv.).	48
7.4 Circular convolution example.	49
7.5 1/3 Simpson's rule error.	49
7.6 Martingality check for the fast method.	50
7.7 Heston CF choice.	50
8 Appendix B: Individual SVI smiles.	52
9 Appendix C: Estimated parameters for RFSV.	53
10 Appendix D: Heston parameters.	54
11 Appendix E: RND check of the calibrated IVS.	55
11.1 RFSV RND.	55
11.1.1 Short-term.	55
11.1.2 Medium-term.	55
11.1.3 OOS.	56
12 Appendix F: Heston RND.	57
13 Appendix G: Prices MAE comparison.	58
13.1 Short-term.	58
13.2 Medium-term.	59
13.3 Out of sample.	60

1 Fractional Brownian Motion.

Figure 1: Animation of the Mandelbrot set, named after the pioneer of the self-similarity theory in natural processes, who first visualized it at IBM in 1980. To visualize it open the PDF with Adobe Acrobat.

Stochastic processes have long been used in financial markets mathematical modeling to represent the inherent uncertainty and randomness in asset price dynamics. Stochastic calculus has served as the basis for quantitative finance since Bachelier's work "Théorie de la spéculation" in 1900 and the subsequent development of the geometric Brownian motion model, that underlies the well-known Black-Scholes equation. The shortcomings of classical Brownian models, however, have been repeatedly demonstrated by empirical data: asset returns show long-range dependence, heavy tails, and volatility clustering, features that are insufficiently explained by the Markovian and memoryless structure of typical stochastic processes.

Models that make use of stochastic volatility, in particular when it is fractional, are a dynamic and strong alternative to classical models. By introducing the Hurst parameter (H), fractional models can reproduce both short and long memory effects, incorporating the persistence and roughness of financial time series. This added flexibility results in more precise volatility modeling, correlation structures, and microstructural effects representation.

With the exception of the trivial case, where the Hurst index equals 0.5, the fBM is not a semimartingale like the standard Brownian motion, a characteristic that makes Ito's calculus ineffective. Furthermore, the fBM is non-local in nature, its increments are not independent, and the process's evolution at a given time t is influenced by the trajectory's whole history up to that point. In other words, because the fractional Wiener process has memory and long-range dependence, it is not Markovian. Even though it makes mathematical analysis more difficult, this inherent non-locality offers a more realistic framework for simulating financial time series where past dynamics have a big impact on future behavior.

Fractional processes have been used in financial modeling to explain the persistence of correlation structures across asset classes, the roughness of equity market volatility and long-term dependence in interest rates. According to recent empirical findings volatility exhibits anti-persistent dynamics and behaves more like a process where the Hurst parameter is less than 0.5; we refer to the "rough volatility" literature. Rough fractional stochastic volatility models have been developed as a result and they perform better than classical stochastic volatility models in terms of both calibration accuracy and predictive power.

This thesis is devoted to the study of fractional stochastic processes and their applications to the mathematical modeling of financial assets.

In the first section we provide an overview of the theoretical framework emphasizing the construction, main characteristics and statistical properties of the fractional Brownian motion. The Rough Fractional Stochastic Volatility (RFSV) model, which is the main contribution of this work, is introduced in Section 2 along with the Heston model, which serves as a comparison point. The statistical characterization of the dataset, including an explanation of its key attributes and the derivation of a smooth and precisely defined objective function for model calibration is covered in Section 3. The estimation methodology is covered in detail in Section 4, which also discusses how we handle the transition between probability measures and outlines our suggested two-measure estimation approach: the \mathbb{P} -measure, which is used for the statistical estimation of the Hurst parameter and the \mathbb{Q} -measure, which is used for the calibration of the remaining parameters under the risk-neutral framework for pricing purposes. The empirical results and important conclusions drawn from the calibration and validation exercises are finally presented and discussed in Section 5.

1.1 Fractional Brownian Motion.

Fractional Brownian motion, introduced by [1], is a family of Gaussian processes extending classical Brownian motion through the Hurst parameter H . Unlike the standard version it shows dependence between increments, encoding memory and long-range effects. These features, together with its self-similarity, make it a natural candidate for modeling financial time series, where past dynamics influence future behavior. The index H is the driver of the memory effect; if we have an index $H < 1/2$, the sample paths of the fractional Brownian motion become rougher, reflecting anti-persistent behavior. In practical terms this means that the process tends to revert after deviations, creating a mean-reverting effect. However, unlike classical mean-reverting processes, this reversion is not toward a fixed, time-homogeneous level, but rather toward a dynamic reference that may evolve over time. When $H > 1/2$ the process behaves in a persistent manner and the dependence has long-range effects. In this regime positive increments are more likely to be followed by positive increments (and negative by negative), leading to a smoother trajectory compared to the standard Brownian motion. This behavior reflects a form of trend reinforcement, where past movements increase the likelihood of similar future dynamics, a feature often observed in long-memory phenomena such as volatility clustering in financial markets.

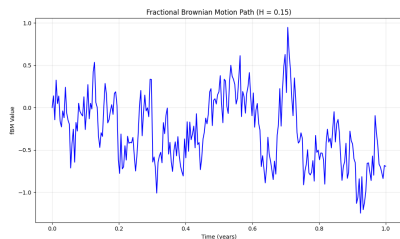


Figure 2: Rough fBM.

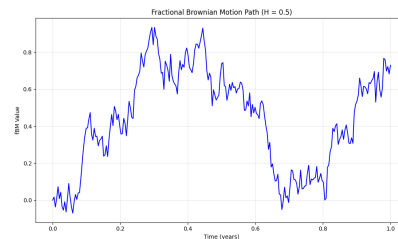


Figure 3: The trivial case.

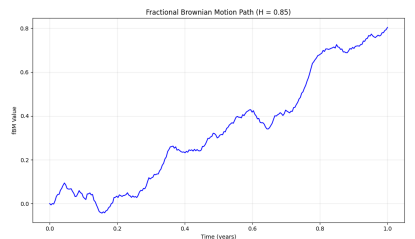


Figure 4: Long-memory fBM.

We define a process, W , Gaussian if: $\forall t \in [t_1, t_n]$ the series $\{W_{t_1}, \dots, W_T\}$ has a multivariate Normal

distribution. Moreover, if $\mathbb{E}[W] = 0$ and the covariance function is of the form:

$$\gamma_{W^H}(s, t) = \mathbb{E}[W_t^H W_s^H] - \mathbb{E}[W_t^H] \mathbb{E}[W_s^H] = \frac{1}{2}(t^{2H} + s^{2H} - |t - s|^{2H}).$$

We can call W_t^H a fractional Brownian Motion with hurst exponent H , $H \in (0, 1)$. The distribution of a Gaussian process is fully characterized by its mean and covariance. Nevertheless, to guarantee the existence of such process we should add another condition, we must have an autocovariance matrix defined as:

$$\Sigma = [\gamma_h(t_i, t_j)]_{i,j}^n.$$

That must be positive semi-definite:

$$\Sigma \text{ is positive semi-definite} \iff x^T \Sigma x \geq 0 \quad \forall x \in \mathbb{R}^n \quad (1)$$

Proof in Appendix A.

1.2 Properties of fBM.

We state some properties of the fBM:

- For any $t \geq 0$, $W_t^H \sim \mathcal{N}(0, t^{2H}) \implies W_t^H \sim t^H Z$ where $Z \sim \mathcal{N}(0, 1)$. The p-th moment of W_t^H is then $\mathbb{E}[(W_T^H)^p] = t^{pH} \mathbb{E}[(Z)^p]$ and the moments exists for all the p even and greater than zero and their value is given by $\mathbb{E}[(Z)^p] = \frac{(2k)!}{2^k k!} = (2k-1)!!$, $p = 2k$.
- The process is continuous a.e. and it enjoys the self-similarity property: for $a > 0$, $W_{at}^H \stackrel{d}{=} a^H W_t^H$, $\forall t > 0$.
- The sample path of W_T^H are α -Hölder continuous in each compact set, $\forall \alpha \in (0, H)$ and $H \leq 1$, this means the paths are "smooth" as $\alpha < H$ in the sense that $|f(t) - f(s)| \leq C|t - s|^\alpha \quad \forall (t, s) \in [0, n]$.
- As we already stated, for $H \neq \frac{1}{2}$, W^H has dependent increments, it is not a martingale (nor a semi-martingale) and it is not Markovian.
- The increments are characterized by:

$$\begin{aligned} \mathbb{E}[(W_t^H - W_s^H)^2] &= \mathbb{E}[(W_t^H)^2] + \mathbb{E}[(W_s^H)^2] - 2\gamma_H(t, s) = t^{2H} + s^{2H} - (t^{2H} + s^{2H} - |t - s|^{2H}) = \\ &= |t - s|^{2H} \end{aligned}$$

from which it follows that $W_t^H - W_s^H \sim \mathcal{N}(0, |t - s|^{2H})$, therefore this difference is stationary since it depends only on $k = |t - s|$. Moreover, a useful scaling property is the following: $\mathbb{E}[|W_{t+\Delta}^H - W_t^H|^q] \propto \Delta^{qH}$.

- Define $D_n := W_n^H - W_{n-1}^H$, obviously $D_n \sim \mathcal{N}(0, 1) \quad \forall n$, so $\{D_n\}_{n>0}$ is a sequence of identical distributed but not trivially independent random variables. Then:

$$\begin{aligned}\gamma_D(n, n+k) &= \mathbb{E}[D_n D_{n+k}] - \mathbb{E}[D_n] \mathbb{E}[D_{n+k}] = \mathbb{E}[(W_n^H - W_{n-1}^H)(W_{n+k}^H - W_{n+k-1}^H)] = \\ &= \gamma_{W^H}(n, n+k) - \gamma_{W^H}(n, n+k-1) - \gamma_{W^H}(n-1, n+k) + \gamma_{W^H}(n-1, n+k-1) = \\ &= \frac{1}{2} [|k+1|^{2H} + |k-1|^{2H} - 2|k|^{2H}]\end{aligned}$$

With the asymptotic:

$$\gamma_D(n, n+k) \underset{k \uparrow \infty}{\sim} H(2H-1)k^{2H-2}$$

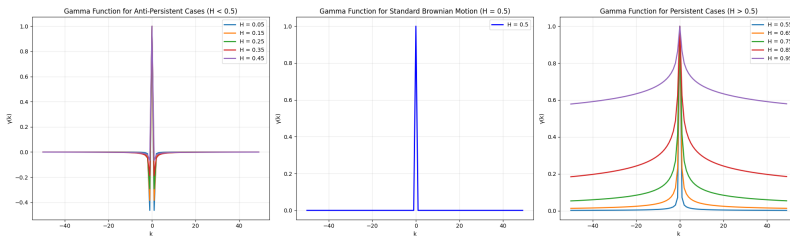


Figure 5: $\gamma_D(n, n+k)$ for some H .

We can see how for each of the cases the value $\gamma(0) = 1$ as it should, for the case $H < 0.5$ the ACF plot is negative for all nonzero lags, although this effect is limited. In fact, it is possible to prove that $\sum_{k=1}^{\infty} \gamma_D(n, n+k) < \infty$. As result the process behaves as we discussed above: it is mean-reverting in the short run but the mean level to which it reverts towards changes over time. The process is then called anti-persistent or more friendly, rough.

For $H > 0.5$ the ACF is positive for all lags, and moreover it is possible to prove that $\sum_{k=1}^{\infty} \gamma_D(n, n+k) = \infty$ which generates the long-memory effect. This makes the process effectively trending, a behavior commonly referred to as persistence.

For $H = 0.5$ we deduce that the increments are effectively independent since the plot takes only the value of 0.

1.3 Construction of fBM.

Let $\{W_t\}_{t \geq 0}$ be the standard Wiener process, onto the usual \mathbb{P} -measure space, $(\Omega, \mathcal{F}, \mathbb{P})$ with σ -algebra defined by the augmented filtration $\{\mathcal{F}_t\}_{t \geq 0}$ generated by W . Then:

$$W_t^H = a_H \int_{\mathbb{R}} [(t-s)_+^{H-1/2} - (-s)_+^{H-1/2}] dW_s, \quad (n)_+ := n \vee 0$$

is a fBM existing $\forall t \in \mathbb{R}$ and $H \in (0, 1)$. Moreover, a_H is a normalizing constant chosen to make $\mathbb{E}[W_s W_t] = \gamma_{W^H}(s, t)$, that can take form of this type:

$$a_H = \left\{ \frac{1}{2H} + \int_{\mathbb{R}^+} [(1+u)^{H-1/2} - u^{H-1/2}]^2 du \right\}^{-1/2} = \frac{\sqrt{2H \sin(\pi H) \Gamma(2H)}}{\Gamma(H+1/2)}, \quad 0 < a_H < \infty$$

look, for example, at [2], and the kernel $g_t^{MvN}(s) = [(t-s)_+^{H-1/2} - (-s)_+^{H-1/2}]$ is called Mandelbrot van Ness kernel [1].

Another kernel specification was introduced by Lévy [3], $g_t^L(s) = (t-s)^{H-1/2}$, yielding:

$$Z_t^H = b_H \int_0^t (t-s)^{H-1/2} dW_s$$

where b_H is chosen to be $b_H = \sqrt{2H}$.

We can find the conditional law of W_t^H given its history up to time u , $0 \leq u \leq t$ by:

$$\mathbb{E}[W_t^H | \mathcal{F}_u^W] = W_t^H - a_H \int_u^t (t-s)^{H-1/2} dW_s$$

this implies that the conditional distribution takes the form:

$$W_t^H | \mathcal{F}_u^W \sim \mathcal{N}(\mathbb{E}[W_t^H | \mathcal{F}_u^W], \frac{a_H^2}{2H} (t-u)^{2H})$$

2 The models.

In this section we give the presentation of the stochastic volatility models considered in this work. We start by discussing the motivation and the need for stochastic volatility, highlighting its role in capturing key empirical features of financial data that constant volatility models fail to explain.

Then, we introduce the Ornstein-Uhlenbeck (OU) process, this serves as the foundational building block of mean-reverting dynamics in volatility modeling. This framework is then extended to the fractional version of the latter, which is the fractional Ornstein–Uhlenbeck (fOU) process, with this it is possible to include long-memory effects to better represents the roughness (or persistence) that one can observe in financial markets.

In the following we present the model proposed in [4], this combines the above elements into a coherent framework driven by a fOU process. The section details the mathematical depiction of the model and its main properties, setting the basis for the analysis developed afterward.

Finally, to have a comparison of the "goodness" of this model, we introduce the Heston equation, that will be used as a benchmark.

2.1 Theoretical setting.

The following is taken from [4] and [5]. It is a well-known fact that, under the Black–Scholes (1973) model, all implied volatilities for options on the same underlying asset should coincide with the model's constant volatility parameter. In practice, however, this does not hold: implied volatility varies with calendar time, time to maturity, and the option's moneyness. These variations produce the well-known volatility smile or skew, reflecting systematic deviations of market option prices from the theoretical values prescribed by the Black–Scholes framework. It is now widely recognized that these patterns can be explained, at least in part, by acknowledging that volatility is itself stochastic. Essential studies such as [6], [7], and [8] introduced models in which instantaneous volatility evolves as a random process, giving rise to the general stochastic volatility (SV) framework:

$$\frac{dS_t}{S_t} = \mu(t, S_t)dt + \sigma_t dW_t^{(a)}$$

where S_t is the evolution of the modeled asset and σ_t is the instantaneous volatility, that moves as:

$$dV_t = k(\theta - V_t)dt + \nu dW_t^{(2)}$$

in which $V_t = \ln(\sigma_t)$ and the pair $(W_t^{(a)}, W_t^{(2)})$ is a non degenerate bivariate Wiener process with $\mathbb{E}[W_t^{(a)}W_t^{(2)}] = \rho$. V_t is assumed to satisfy an OU process leading to stationary volatility dynamics. This simple specification generalises the, constant volatility, Black–Scholes model while remaining analytically tractable and preserving the semimartingale behaviour of the price process. Such models reproduce a number of empirical regularities which are seen in the options market, such as volatility clustering and leverage effects; they lead naturally to implied volatility surfaces that do not lie flat on a plane. Giving one example, the Hull-White model can be interpreted as finding the European options price using the

Black and Scholes formula but substituting the fixed volatility with:

$$\sigma_{t,T}^2 = \frac{1}{T-t} \int_t^T \sigma^2(u) du$$

and where the expectation is found with respect to the conditional probability distribution of $\sigma_{t,T}^2$ given σ_t . Or again, the slightly more recent Heston model [9], where the volatility moves as the CIR process:

$$d\sigma_t = k(\theta - \sigma_t)dt + v\sqrt{\sigma_t}dW_t^{(2)}$$

However, high-frequency data reveal that volatility fluctuations occur on very fine time scales and display a degree of irregularity incompatible with classical diffusion-based stochastic volatility models. This has led to an ongoing debate regarding the true nature of volatility persistence. While some authors [4] and [10] interpret volatility persistence as evidence of persistent behavior, others [11] argue that volatility should instead be modeled as a rough process, with trajectories that are less regular than those of the standard Brownian motion.

2.1.1 Ornstein-Uhlenbeck.

The classical OU process, with some parameters $(\lambda, \sigma) > 0$ and starting at some $x \in \mathbb{R}$, is the unique strong solution of the Langevin equation with Wiener noise:

$$X_t = \xi - \lambda \int_0^t X_s ds + \sigma W_t, \quad t \geq 0$$

and ξ is just the initial condition x , that makes the solution unique. It is given by the (a.e.) continuous Gaussian Markov process:

$$Y_t(x) := e^{-\lambda t}(x + \sigma \int_0^t e^{\lambda u} dW_u), \quad t \geq 0$$

This yields that the unique strong solution for X_t , with the initial condition:

$$\xi = \sigma \int_{-\infty}^0 e^{\lambda u} dW_u$$

arises from the condition of non-negative t 's of the stationary, centered and (a.e.) continuous Gaussian Markov process:

$$Y_t := \sigma \int_{-\infty}^t e^{-\lambda(t-u)} dW_u, \quad t \in \mathbb{R}$$

It can be checked the following:

$$\gamma_t(t, t+s) := \text{Cov}(Y_t, Y_{t+s}) = \frac{\sigma^2}{2\lambda} e^{-\lambda|s|}, \quad (t, s) \in \mathbb{R}$$

this implies the subsequent: Y_t is an ergodic process and furthermore:

$$Y_t - Y_t(x) = \sigma \int_{-\infty}^t e^{-\lambda(t-u)} dW_u - e^{-\lambda t}(x + \sigma \int_0^t e^{\lambda u} dW_u) = e^{-\lambda t}(Y_0 - x)$$

if we check the asymptotic behavior of $Z_t := e^{-\lambda t}(Y_0 - x)$ we obtain:

$$Z_t \xrightarrow{t \uparrow \infty} 0, \quad \text{a.s.}$$

this is simply because the deterministic exponent converges toward 0 as t grows and $Y_0 - x$ is an L^2 random variable.

2.1.2 Fractional Ornstein-Uhlenbeck.

Let $(\lambda, \sigma) > 0$ and $\xi \in L^0(\Omega)$, Ω being the usual sample space . Considering that the Langevin equation:

$$X_t = \xi - \lambda \int_0^t X_s ds + N_t, \quad t \geq 0$$

only requires an integral with respect to t , it can be solved path-wise for much more broad noise process $\{N_t\}_{t \geq 0}$ than the classical Brownian motion. Take as an example:

$$\int_a^t e^{\lambda u} dW_u^H, \quad t > a$$

the above, for each $H \in (0, 1]$ and for every $a \in [-\infty, \infty)$, exists as a path-wise integral of the Riemann-Stieltjes type, moreover:

$$Y_t^H(\xi) := e^{-\lambda t} (\xi + \sigma \int_0^t e^{\lambda u} dW_u^H), \quad t \geq 0$$

is the unique (a.e.) continuous process that solves:

$$X_t^H = \xi - \lambda \int_0^t X_s ds + \sigma W_t^H, \quad t \geq 0.$$

Specifically, the restriction to positive t of the process:

$$Y_t^H := \sigma \int_{-\infty}^t e^{-\lambda(t-u)} dW_u^H, \quad t \in \mathbb{R}$$

solves X_t^H with initial condition $\xi = Y_0^H$. From this it follows that, even in the fractional case, $Z_t^H := Y_t^H - Y_t^H(\xi) = e^{-\lambda t} (Y_0^H - \xi)$ behaves in the following way:

$$Z_t^H \xrightarrow{t \uparrow \infty} 0, \quad \text{a.s.}$$

this implies that every stationary solution of X_t^H has the same distribution of $\{Y_t^H\}_{t \geq 0}$. We then call $\{Y_t^H(\xi)\}_{t \geq 0}$ a fractional OU process with initial condition ξ and $\{Y_t^H\}_{t \in \mathbb{R}}$ the stationary version of the latter.

2.2 The Fractional Stochastic Volatility Model.

The Fractional Stochastic Volatility (FSV) model, originally introduced by [4], extends the classical Hull–White stochastic volatility framework by allowing the volatility process to be driven by a fractional Brownian motion. This modification enables the model to reproduce long-range dependence and persistence when modeling volatility, while maintaining a continuous-time setting compatible with arbitrage-free asset price dynamics. In the FSV framework the logarithm of the instantaneous volatility follows a fOU process, which generalizes the standard OU dynamics by incorporating memory through the Hurst exponent. In the formulation of [4], the memory parameter is expressed in terms of an auxiliary parameter α , via the function:

$$\alpha = H - 1/2 \quad \text{or equivalently} \quad H = \alpha + 1/2$$

To model long-range persistency, which corresponds to $H \in (\frac{1}{2}, 1)$ Comte and Renault restrict the parameter to the range $0 < \alpha < \frac{1}{2}$. In contrast, adopting the empirical perspective of [11], where volatility is found to be rough, rather than persistent, we will consider the opposite regime $-\frac{1}{2} < \alpha < 0$ which corresponds to $H \in (0, \frac{1}{2})$.

2.2.1 The Long-Memory process.

Consider the first order fractional SDE:

$$dX_t = -kX_t dt + \gamma dW_t^\alpha, \quad X_0 = 0, \quad k > 0, \quad 0 < \alpha < \frac{1}{2}. \quad (2)$$

Where the solution can be written as in [12]:

$$X_t = \int_0^t e^{-k(t-s)} \gamma dW_s^\alpha$$

We know that integrating with respect to a fBM is defined only in the Wiener L^2 sense and only for deterministic functions. We then obtain a family of Gaussian processes. X_t can be written also as:

$$\int_0^t f(t-s) dW_s$$

with:

$$\begin{aligned} f(x) &= \frac{\gamma}{\Gamma(1+\alpha)} \frac{\partial}{\partial x} \int_0^x e^{-ku} (x-u)^\alpha du = \\ &= \frac{\gamma}{\Gamma(1+\alpha)} (x^\alpha - k e^{-kx} \int_0^x e^{ku} u^\alpha du) \end{aligned} \quad (3)$$

Notice how, here, we have the Gamma function in the denominator, this is not a problem for the kernel even if we use our claim that $\alpha \in (-\frac{1}{2}, 0)$; the Γ function is well behaved and monotonically decreasing in the interval $(1 - \frac{1}{2}, 1)$. In particular, it takes the values: $\Gamma(1 - \frac{1}{2}) = \sqrt{\pi} \approx 1.7724$ and $\Gamma(1) = 1$. We have the stationary version of X_t :

$$Y_t = \int_{-\infty}^t f(t-s) dW_s$$

this implies that the solution, X , is given by:

$$X_t = \int_0^t \frac{(t-s)^\alpha}{\Gamma(1+\alpha)} dX_s^{(\alpha)}$$

where the α -th order derivative is:

$$X_t^{(\alpha)} = \frac{\partial}{\partial t} \int_0^t \frac{(t-s)^{-\alpha}}{\Gamma(1-\alpha)} = \int_0^t e^{-k(t-s)} \gamma dW_s$$

There exists also the general (continuous) spectral density of processes in the solution family of dX_t :

$$p^c(\omega) = \frac{\gamma^2}{\Gamma(1+\alpha)^2 \omega^{2\alpha} (\omega^2 + k^2)}$$

The family of long-memory processes, as proved in [12], enjoys the following properties:

- The covariance function $\gamma_Y(s, t)$, associated with X , has the following asymptotic for $h \rightarrow 0$ and ψ fixed:

$$\gamma_Y(t, t+h) = \gamma_Y(0) + \frac{1}{2} \psi |h|^{2\alpha+1} + o(|h|^{2\alpha+1})$$

- X is ergodic in the L^2 sense, see also above.
- There exists a process Z_t that coincide a.e. to X_t , such that the sample function of Z satisfies the Lipschitz condition of order β , $\forall \beta \in (0, \alpha + \frac{1}{2})$.

All the above imply that the greater (smaller) the α value is, the smoother (rougher) the path of the process is.

2.2.2 Statistical properties of σ_t in the FSV model.

The main assumption in the strategy of [4] is to suppose that the solution of (2) is the logarithm of the stochastic volatility, $X_t = \ln(\sigma_t)$. The volatility process is then asymptotically equivalent, in the L^2 sense, to the stationary process:

$$\tilde{\sigma}_t = \exp\left\{\int_{-\infty}^t e^{-k(t-s)} \gamma dW_s^{\alpha, (2)}\right\}, \quad k > 0, \quad 0 < \alpha < \frac{1}{2}.$$

Moreover, the volatility process is assumed to be asymptotically stationary and nowhere differentiable. The fractional exponent α provides some degree of freedom in selecting the regularity of the path. Actually, it is possible to show that σ_t has the same type of regularity property as the fractional process $X_t = \ln(\sigma_t)$.

2.2.3 Discretization of the model.

The objective of this chapter is to introduce the numerical methods used to implement the stochastic process presented above. In particular we discuss the discretization and the integration scheme used to approximate the continuous-time version of that model. Due to the fact that an analytical solution is not available for this particular SDE, the numerical aspect is even more important to simulate faithful and coherent paths.

From the previous sections we know that the solution for (2) is the integral expression:

$$X_t = \int_0^t \frac{(t-s)^\alpha}{\Gamma(1+\alpha)} dX_s^{(\alpha)} = \int_0^t f(t-s) dW_s^{(2)}$$

in which $f(x)$ is given in (3). A natural discretization of the above is through the usage of step functions. We only use the value of the involved processes $(X_s^{(\alpha)}, W_s^{(2)})$ on a discrete partition of $[0, t]$: j/n , $j = 0, 1, \dots, [nt]$ that yields:

$$X_{n,t} = \int_0^t \frac{(t - \frac{[ns]}{n})^\alpha}{\Gamma(1+\alpha)} dX_s^{(\alpha)} \quad \text{and} \quad X_{n,t} = \int_0^t f(t - \frac{[ns]}{n}) dW_s^{(2)}$$

which gives:

$$\hat{X}_{n,t} = \sum_{j=1}^{[nt]} \frac{(t - \frac{j-1}{n})^\alpha}{\Gamma(1+\alpha)} \Delta X_{(\frac{j}{n})}^{(\alpha)} \quad \text{and} \quad \tilde{X}_{n,t} = \sum_{j=1}^{[nt]} f(t - \frac{j-1}{n}) \Delta W_{(\frac{j}{n})}^{(2)}$$

With the following notation convention:

$$\Delta X_{(\frac{j}{n})}^{(\alpha)} = X_{(\frac{j}{n})}^{(\alpha)} - X_{(\frac{j-1}{n})}^{(\alpha)} \quad \text{and} \quad \Delta W_{(\frac{j}{n})}^{(2)} = W_{(\frac{j}{n})}^{(2)} - W_{(\frac{j-1}{n})}^{(2)}$$

It is proven that those approximations converge in distribution, in the sense of [13], to the stationary process X . The $\tilde{X}_{n,t}$ is the most mathematically tractable, and it is the one that will be used in the following.

2.2.4 The Global Filtering Model.

To fully simulate the model we need to approximate also the price movement, S_t , if we set $Y_t = \ln(S_t)$ and $V_t = \ln(\sigma_t)$ we get the following dynamics:

$$\begin{cases} dY_t = \sigma_t dW_t^{(1)} \\ dV_t = -kV_t dt + \gamma dW_t^{(2),\alpha} \end{cases}$$

where again $(W^{(1)}, W^{(2),\alpha})$ are a pair of non degenerate Wiener process, $W^{(2),\alpha}$ is fractional with index α , their correlation is $\mathbb{E}[W^{(1)}, W^{(2),\alpha}] = \rho$ and $-1 < \rho < 1$ but usually $-1 < \rho < 0$. By similar arguments of the volatility discretization, we have the following:

$$\begin{aligned} Y_{n,t} &= \int_0^t \sigma_{(\frac{[ns]}{n})} dW_s^{(1)} = \\ &= \sum_{j=1}^{[nt]} \sigma_{(\frac{j-1}{n})} \Delta W_{(\frac{j}{n})}^{(1)} + \sigma_{(\frac{[nt]}{n})} (W_t^{(1)} - W_{(\frac{[nt]}{n})}^{(1)}) \end{aligned}$$

from which we obtain the more easily computable version:

$$\begin{aligned} \tilde{\sigma}_{n,t} &= \exp \left\{ \sum_{j=1}^{[nt]} f(t - \frac{j-1}{n}) \Delta W_{(\frac{j}{n})}^{(2)} \right\}, \\ \tilde{Y}_{n,t} &= \sum_{j=1}^{[nt]} \tilde{\sigma}_{n,(\frac{j-1}{n})} \Delta W_{(\frac{j}{n})}^{(1)} \end{aligned}$$

Then in [4], the following proposition is proven:

$$\begin{bmatrix} \tilde{Y}_n \\ \tilde{\sigma}_n \end{bmatrix} \xrightarrow{D} \begin{bmatrix} Y \\ \sigma \end{bmatrix} \xrightarrow{n \uparrow \infty} \begin{bmatrix} \tilde{S}_n = \exp\{\tilde{Y}_n\} \\ \tilde{\sigma}_n \end{bmatrix} \xrightarrow{D} \begin{bmatrix} S \\ \sigma \end{bmatrix}$$

Note how in the discretization of the volatility we have a Volterra type convolution between $f(x)$ and the Wiener process observation.

2.2.5 Integration scheme.

Now to simplify things, $\Delta W_{(\frac{j}{n})}^{(i)}$ is just the increment of the i -th Brownian, in our case just $N(0, dt)$, the two Brownians can be correlated with ρ , we simply apply Cholesky:

$$W^{(2),\text{corr}} = \rho \cdot W^{(1)} + \sqrt{1 - \rho^2} \cdot W^{(2),\perp}.$$

So, when $n \rightarrow \infty$:

$$\text{Var}(V_{n,t}) = \text{Var}\left(\sum_{j=1}^{[nt]} f(t - \frac{j-1}{n}) \Delta W_{(\frac{j}{n})}^{(2)}\right) = \frac{1}{n} \sum_{j=1}^{[nt]} f^2(t - \frac{j-1}{n}) \underset{n \rightarrow \infty}{\sim} \int_0^t f^2(t-s) ds$$

and that is the variance of:

$$\int_0^t f(t-s) dW_s^{(2)}$$

This is just a Volterra convolution; where the kernel is $f(n)$ and the function we weight are the Brownian increments, the more recent increment is weighted with the "oldest" $f(n)$. If we want the scheme to work under \mathbb{Q} , we need to make S_t a martingale, and since $Y_t = \ln(S_t)$ we obtain:

$$S_t = S_0 \cdot \left(\exp\left\{\int_0^t \sigma_{(s)} dW_s^{(1)} - \frac{1}{2} \int_0^t \sigma_{(s)}^2 ds\right\} \right) \quad (4)$$

the proof is given in Appendix A.

The first and simplest scheme we propose is the following, we use it to show the martingale property and the behavior of the model as we change α . A more refined and computationally faster version will be given in the parameters estimation section.

The process of the log price is integrated via Euler-Maruyama:

$$Y_{t+\Delta t} = Y_t + (r - q - \frac{1}{2} \sigma_t^2) \Delta t + \sigma_t \Delta W_t^{(1)}$$

instead the log-vol process is just a discrete Volterra convolution using a left-Riemann sum.

$$V_i \approx \sum_{k=0}^i f(t_i - t_k) \Delta W_k^{(2)}$$

The integral inside the $f(x)$ is computed numerically through quadrature (implemented via the scipy library).

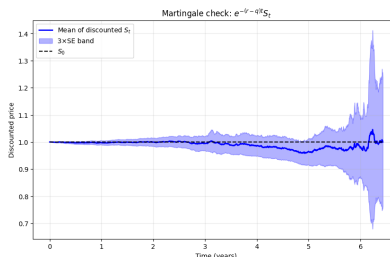


Figure 6: The mean S_t path, for 250'000 trajectories, with $(\gamma, k, \alpha, \rho) = (0.01, 1, 0.2, 0)$.

What we just plotted is the time-series of the discounted expected price evolution from a Monte Carlo simulation with our scheme. The dark blue line represents the mean path, and the light blue bands are the Monte Carlo error computed as:

$$\text{MC}_{\text{err}} = \bar{S}_t \pm \frac{3 \cdot \text{SD}(S_t)}{\sqrt{M}}$$

S_t is the vector of simulated paths at time t , it has dimension $M = 250'000$, that is the number of trajectories, \bar{S}_t is its mean and $\text{SD}(S_t)$ the standard deviation.

Below we propose the plots of the vol path for different values of α :

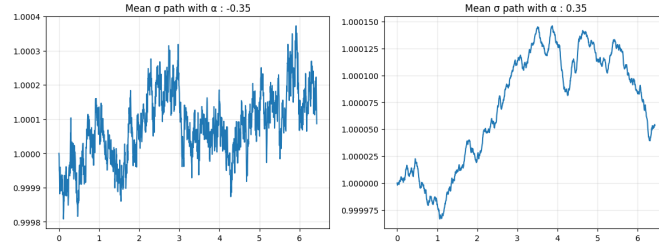


Figure 7: The mean σ_t path with $(\gamma, k, \alpha, \rho) = (0.01, 1, 0.2, 0)$ for $\alpha = -0.35$ and $\alpha = 0.35$.

2.3 The Heston model.

A fundamental component of contemporary quantitative finance is the Heston model [9], a classical stochastic volatility model. By adding a mean-reverting stochastic process for the variance, it expands on the Black-Scholes framework and enables it to account for important market characteristics like the leverage effect and the volatility smile. The Heston model's ability to replicate the roughness seen in empirical volatility time series is limited by its assumption of smooth volatility dynamics, despite its success and analytical tractability. This thesis will highlight the distinctions between the classical and rough approaches to volatility modeling by comparing the proposed RFSV model to the Heston model. In this section we will swiftly introduce the equation and then in Section 4.4.2 we will show the computational and calibration procedures.

2.3.1 The Heston equation.

The Heston model assumes that S_t evolves like:

$$\frac{dS_t}{S_t} = \mu dt + \sqrt{v_t} dW_t^{(1)}$$

where the volatility process $\sqrt{v_t}$ moves like a square root CIR process:

$$dv_t = \kappa(\theta - v_t)dt + \xi \sqrt{v_t} dW_t^{(2)}$$

where $(W^{(1)}, W^{(2)})$ are the, non trivially correlated, Wiener processes. The parameters of the volatility process need to obey the following condition (Feller), in order to make v_t strictly positive:

$$2\kappa\theta > \xi^2$$

3 Statistical Description and Volatility Surface Smoothing.

This chapter is comprised of two significant sections. The first section describes the Euro Stoxx 600 futures market, using statistical methods to analyze the empirical properties of the underlying price data. Because an index is not something one can directly trade, we will use the most liquid futures for each trading moment. We have minute-by-minute price observations, which allow us to view market behavior at high frequency and undertake analysis of short-run volatility, intraday patterns, and other distributional properties of returns.

The second part of the chapter elaborates on the construction and smoothing of the derived volatility surface from the options market chain. Observed implied volatilities are generally irregular and often contaminated by noise from the market. Therefore, if we simply interpolate observed implied volatilities, we can create inconsistencies and potential arbitrage opportunities if the market does not price options consistently. To solve this issue we introduce the Stochastic Volatility Implied (SVI), an arbitrage free and parametric model that makes the surface more tractable.

3.1 Data Description.

3.1.1 Price series.

The data we chose to utilize were retrieved from the LSEG platform, Refinitiv. The data used, in a manner similar to [11], consist of the minute-by-minute price series of the futures written on the Euro Stoxx 600. Those spanned from 23/09/2024 to 19/09/2025.

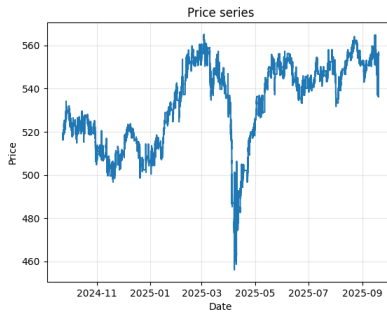


Figure 8: S_t series for the most liquid futures on Stoxx 600 at each given moment.

From which we obtain the following basic statistics from the usual log returns: $r_t = \ln(\frac{S_t}{S_{t-1}})$, resampled at the daily frequency for better treatment:

Table 1: Daily Log-Return Statistics

Statistic	Value
Mean	-0.000303
Skewness	1.044555
Excess Kurtosis	16.878424

And the following plot for the distribution:

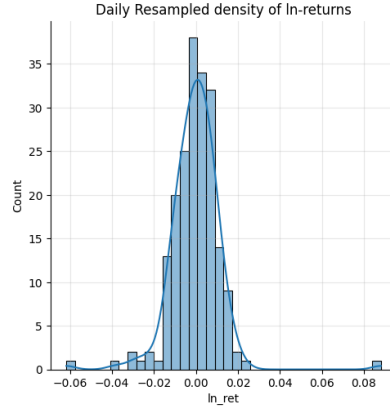


Figure 9: $\ln\left(\frac{S_t}{S_{t-1}}\right)$ distribution plot for daily resampled data.

3.1.2 Options chain.

For the options chain we took the data for calls present in the market on 19/09/2025. After some basic cleaning the times to maturity for those spanned from 0.11 to 6.17 years.

The first thing we had to do was to handle the forward modeling; in fact, the SVI parametrization works easily in the forward space. To do this we took (again from LSEG) the ESTR OIS, proxying the risk-free interest, as of the 19/09/2025. Conveniently we already had the discount factor series for various maturities $P(0, T)$; to adapt this to the maturities in the options chain, we did interpolation in log space to get the $P(0, T^*)$ for each T^* in our option retrieved maturities list, so for any $T^* \in [T_s, T_n]$ where $T_{n,s}$ are the maturities present in the discount curve above we did:

$$\begin{aligned}\ln P(0, T^*) &= \ln P(0, T_s) + \frac{T^* - T_s}{T_n - T_s} (\ln P(0, T_n) - \ln P(0, T_s)), \\ P(0, T^*) &= \exp(\ln P(0, T^*))\end{aligned}$$

here we interpolated in the log space making the (simplest) assumption of no arbitrage, coming from:

$$P(0, T) = e^{-\int_0^T r(s)ds} \implies \ln(P(0, T)) = -\int_0^T r(s)ds$$

So, when interpolating in $\ln P(0, T)$ we assume that $r(s)$, the forward rate, is piecewise constant. This ensures that: $P(0, T)$ is strictly decreasing in T , $r(s)$ stays positive and no arbitrage arises.

Having our discount factor we can find the log-moneyness (κ) for each option.

$$\kappa = \ln\left(\frac{K}{\text{fwd}}\right)$$

where K is the traded strike and $\text{fwd} = \frac{S_0}{P(0, T^*)}$.

3.2 Objective function: fitting the SVI.

A popular parametric model to characterize the implied volatility surface of options is the SVI model, which was first presented by [14] in 2004. Its primary objective is to offer a straightforward, yet adaptable, functional form that embodies the common skew and smile patterns seen in implied volatilities across various maturities and strikes. When appropriately constrained the SVI model is especially prized for its arbitrage-free consistency, calibration efficiency, and analytic simplicity. Building smooth implied volatility surfaces, that closely match market data, is a fundamental component for practitioners. In our case it will be essential to find a smooth and complete (in a maturity-moneyness grid sense) surface to find our loss function to use in Section 4.3, that is, we will invert the market implied volatility surface to market implied call prices, using the forward Black formula, to feed in equation 6.

3.2.1 The raw SVI parametrization.

From [14] we know that the parametrization for the total implied variance is:

$$\omega(\kappa, T) := \sigma_{\text{impl}, \kappa}^2 T = a + b[\rho(\kappa - m) + \sqrt{(\kappa - m)^2 + \sigma^2}]$$

- Parameter a : Controls the overall level of variance. An increase in a raises the general variance level, producing a vertical translation of the implied volatility smile. In other words, higher values of a lift the entire smile upward without changing its shape.
- Parameter b : Controls the angle between the asymptotic tails of the smile. If we increase b both wings become steeper, this results in tighter smirks. All of this means that this variable controls how quickly the volatility rises as we move away from the at-the-money level.
- Parameter ρ : It is the parameter that drives the orientation, or skewness, of the smile. When we increase ρ the slope of the left wing decreases and the one of the right increases. This corresponds in a counterclockwise rotation of the smile around its center. Hence, ρ captures the asymmetry between the OTM options.
- Parameter m : This models the horizontal shift of the smile. Increasing m translates the whole smile to the right, indicating the minimum point (usually the ATM region) occurs at a higher strike level.
- Parameter σ : Determines the curvature of the smile near its minimum, the ATM curvature. As σ increases the smile flattens, reducing the curvature at the at-the-money strike. On the contrary, smaller σ lead to a more pronounced and sharper smile.

then to find $\theta = (a, b, \rho, m, \sigma)$ we just need to minimize:

$$f(k, \theta) = \sum_{i=1}^n (\omega_{(i)}^{\text{SVI}} - \omega_{(i)}^{\text{MKT}})^2$$

for each maturity, if we use the bounds coming from [15], which are:

$$\begin{cases} 0 < a < \max \omega^{\text{MKT}}, \\ 0 < b < 1, \\ -1 < \rho < 1, \\ 2 \min \kappa_i < m < 2 \max \kappa_i, \\ 0 < \sigma < 1 \end{cases}$$

it is simply enough to use the "L-BFGS-B" minimization algorithm to find smiles free from butterfly spreads. However, since we are concerned with the fitting of the whole surface another problem to handle is the one of calendar arbitrage. This makes necessary the introduction of a non-linear constraint, that is:

$$q_{\kappa}(x) = w(\kappa, T_i) - w(\kappa, T_{i-1}) \geq 0$$

this means that the total implied variance must be non-decreasing in time to maturity for each moneyness, this ensures the absence of calendar spreads.

The resulting surface is shown below. We chose to include only maturities with $T \geq 0.5$ years, as the shorter maturities tended to be noisy and less reliable.

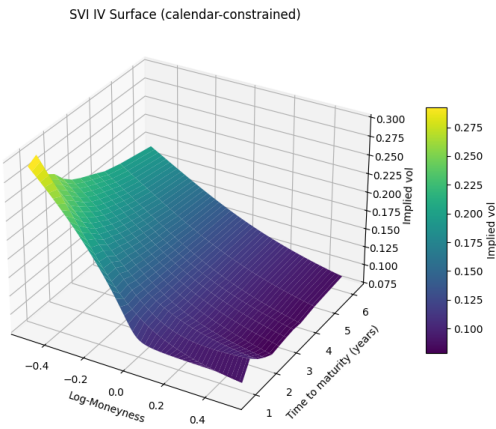


Figure 10: The implied volatility surface for the call market.

To look at the individual smiles fitting, see Section 7.7.

3.2.2 Checking the RND.

From [16] we know the following lemma:

Lemma. A slice is free of butterfly arbitrage if and only if: (1) $g(k) \geq 0$ for all $k \in \mathbb{R}$ and (2) $\lim_{k \rightarrow \infty} d_+(k) = -\infty$.

where,

$$g(k) := \left(1 - \frac{kw'(k)}{2w(k)}\right)^2 - \frac{w'(k)^2}{4} \left(\frac{1}{w(k)} + \frac{1}{4}\right) + \frac{w''(k)}{2} \quad \text{and} \quad d_{\pm}(k) := \frac{-k}{\sqrt{w(k)}} \pm \frac{\sqrt{w(k)}}{2}$$

the first condition makes the risk-neutral density:

$$p(k) = \frac{g(k)}{\sqrt{2\pi\omega(k)}} \exp\left\{-\frac{d_-(k)^2}{2}\right\} \geq 0$$

and the second condition, makes the call price converge to 0 as k goes to infinity. For the proof, see [17]. We plot the RND after numerically verifying that condition (1) is satisfied.

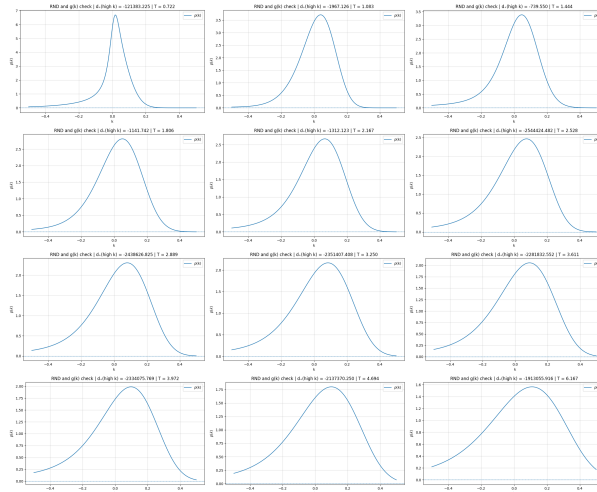


Figure 11: RND for all the considered maturities fitted with the SVI, with the asymptotic of $d_+(k)$.

Moreover, to check the absence of calendar spread, we plot the fitted total implied variance $w(k, T)$ that must be non-decreasing in T :

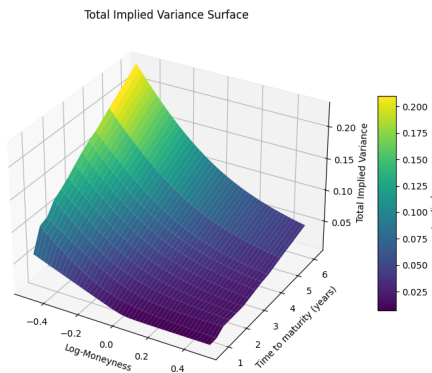


Figure 12: $\sigma_{SVI}^2 T$ to check for the absence of calendar spread.

4 Estimation Methods.

4.1 Realized Volatility Estimation.

Although it cannot be directly observed in market data volatility is a fundamental quantity in financial econometrics. Therefore, rather than being measured, realized volatility needs to be estimated. What we can see are transaction prices, but those are impacted by discreteness, bid-ask bounce and other frictions due to microstructural effects. Rosenbaum's uncertainty zones model [18] offers a strong framework to address these issues by taking into consideration the discrete nature of price fluctuations and microstructural noise. With this method volatility is inferred using precisely crafted estimators that hold true even when market friction effects are present.

4.1.1 Model with uncertainty zones.

Define α to be the tick size (the smallest possible price change), note that this α is not the one introduced earlier, let $k \in \mathbb{N}$ be the "jump" parameter, such that every price change in the time series can be written as a k -multiple of α , let $0 < \eta < 1$ be a parameter that quantifies the aversion to price changes. Then $U_k = [0, \infty) \times (d_k, u_k)$ with:

$$\begin{cases} d_k = (k + 1/2 - \eta)\alpha \\ u_k = (k + 1/2 + \eta)\alpha \end{cases}$$

is the region, around the mid price, called the "uncertainty zone" in which the efficient price cannot trigger a change in the observed price.

This means that U_k is a band around the mid-tick grid value: $(k + \frac{1}{2})\alpha$. When $\eta < 1/2$, there is no overlap between the zones, we will see this later. The main assumption of this model is that the observed price can jump from $k'\alpha$ to $k\alpha$, with $k' \neq k$ if the efficient price crosses the band above or below.

To be precise, we need to give a rigorous definition of the sequence of exit times, $\{\tau_i\}_{i \geq 0}$, from the uncertainty band. Let $\tau_0 = 0$ and $L_0 = 1$, then τ_1 is the exit time of the efficient price $\{X_t\}$ from the set $(d_{k_0-L_0}, u_{k_0+L_0-1})$, $k_0 = \frac{X_0^{(\alpha)}}{\alpha}$ with $X_0^{(\alpha)} := \alpha \cdot \text{round}(\frac{X_0}{\alpha})$ and $\text{round}(x) = \lfloor x + 1/2 \rfloor$. This means that we round X_0 to the nearest multiple of α . We introduce the sequence $\{L_i\}_{i \geq 1}$ of \mathcal{F}_{τ_i} -measurable discrete random variables, which is the absolute value, expressed in number of ticks, of the price jump between the i -th and the $(i+1)$ -th transaction that results in a price change. Next we set, recursively, τ_{i+1} to be:

$$\tau_{i+1} = \inf\{t \mid t > \tau_i, X_t = X_{\tau_i}^{(\alpha)} - \alpha(L_i - \frac{1}{2} + \eta) \text{ or } X_t = X_{\tau_i}^{(\alpha)} + \alpha(L_i - \frac{1}{2} + \eta)\}$$

Specifically, when $X_{\tau_i} = d_j$ for some $j \in \mathbb{N}$, τ_{i+1} is the exit time of $\{X_t\}_{t > \tau_i}$ from the region (d_{j-L_i}, u_{j+L_i-1}) . Conversely, if $X_{\tau_i} = u_j$, always for $j \in \mathbb{N}$, then τ_{i+1} is the escape time from the band (d_{j-L_i+1}, u_{j+L_i}) . Finally, we have:

$$P_{\tau_i} = X_{\tau_i} + \text{sgn}(X_{\tau_i} - X_{\tau_{i-1}})(\frac{1}{2} - \eta)\alpha = X_{\tau_i} + \text{sgn}(P_{\tau_i} - P_{\tau_{i-1}})(\frac{1}{2} - \eta)\alpha$$

from which after estimating η we can estimate X_{τ_i} , see the following sections.

Below we plot the price of the underlying asset for a small time interval, we also include the calculated bands.

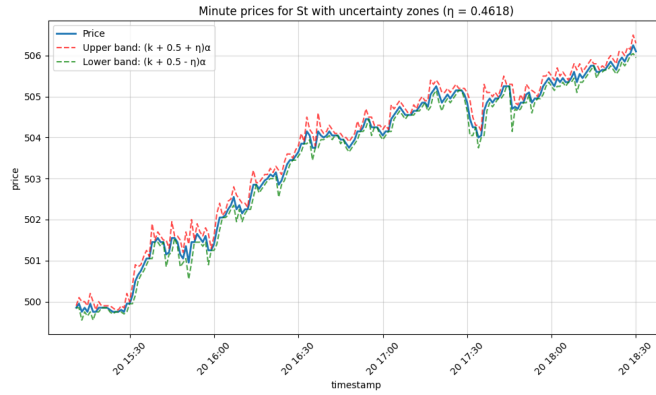


Figure 13: Price trajectory with the associated uncertainty bands for a small interval, on the 20th between 15:00 and 18:30.

Finally, we define the quantities:

$$N_{\alpha,t,k}^{(a)} = \sum_{t_i \leq t} \mathbb{I}_{\{(P_{t_i} - P_{t_{i-1}})(P_{t_{i-1}} - P_{t_{i-2}}) < 0\} \cap \{|P_{t_i} - P_{t_{i-1}}| = k\alpha\}},$$

$$N_{\alpha,t,k}^{(c)} = \sum_{t_i \leq t} \mathbb{I}_{\{(P_{t_i} - P_{t_{i-1}})(P_{t_{i-1}} - P_{t_{i-2}}) > 0\} \cap \{|P_{t_i} - P_{t_{i-1}}| = k\alpha\}}$$

where $N_{\alpha,t,k}^{(a)}$ ($N_{\alpha,t,k}^{(c)}$) counts how many price jumps are alternations (continuations) of k ticks and P_{t_i} indicates the observed price at a time $t_i \leq t$.

4.1.2 Estimation procedure.

Our objective is to find a robust estimator for the integrated variance:

$$IV_t = \int_0^t \sigma_s^2 ds$$

to achieve this, we define the estimator for the realized variance to be:

$$RV_{\alpha,t} := \sum_{\tau_i \leq t} [\ln(X_{\tau_i}) - \ln(X_{\tau_{i-1}})]^2.$$

The X_{t_i} are not directly observable; they take the form:

$$X_{t_i} = P_{t_i} - \alpha(\frac{1}{2} - \eta) \operatorname{sgn}(P_{t_i} - P_{t_{i-1}})$$

the only quantity to estimate is η :

$$\hat{\eta}_{\alpha,t} = (0 \vee \sum_{k=1}^m \lambda_{\alpha,t,k} u_{\alpha,t,k}) \wedge 1$$

with:

$$\lambda_{\alpha,t,k} = \frac{N_{\alpha,t,k}^{(a)} + N_{\alpha,t,k}^{(c)}}{\sum_{j=1}^m [N_{\alpha,t,j}^{(a)} + N_{\alpha,t,j}^{(c)}]} \text{ and } u_{\alpha,t,k} = \frac{1}{2}(k(\frac{N_{\alpha,t,k}^{(c)}}{N_{\alpha,t,k}^{(a)}} - 1) + 1)$$

yielding:

$$\hat{X}_{t_i} = P_{t_i} - \alpha(\frac{1}{2} - \hat{\eta}_{\alpha,t})\text{sgn}(P_{t_i} - P_{t_{i-1}})$$

this will give us, finally, our estimate:

$$\hat{RV}_{\alpha,t} = \sum_{t_i \leq t} [\ln(\hat{X}_{t_i}) - \ln(\hat{X}_{t_{i-1}})]^2.$$

With the claim that:

$$\hat{\eta}_{\alpha,t} \xrightarrow{\text{u.c.p}} \eta \text{ and } \hat{RV}_{\alpha,t} \xrightarrow{\text{u.c.p}} IV_t \text{ as } \alpha \downarrow 0 \quad (5)$$

to see the proof, see the demonstration of Thm. 3.1 in [18].

This estimation gives us the realized variance at the frequency of our price observations (1 minute). To obtain the daily realized variance, we take advantage of the fact that variance is additive across non-overlapping intervals when the "self-arising" effects are cleaned out (the auto-covariance of returns is 0, for all non-zero lags) and simply sum all the minute-by-minute estimates within the same day.

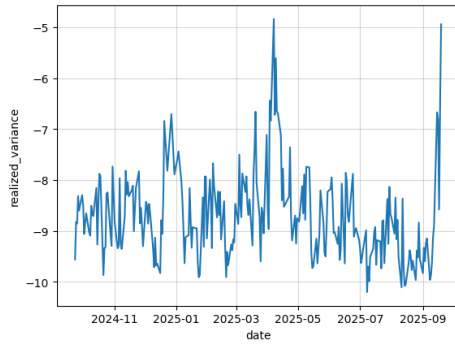


Figure 14: Daily observation of $\ln(\hat{RV}_t)$.

From this point onward, this daily realized variance will serve as our empirical proxy for the process volatility throughout the remainder of the analysis.

Quantity	Estimate
$\hat{\eta}$	0.46181
\hat{RV} (whole series)	0.06901
$\hat{\sigma}$ (whole series)	0.26271

Table 2: \hat{RV} parameters.

Then we can also look at the distribution of the log-volatility increments; it is a stylized fact for them to be Gaussian:

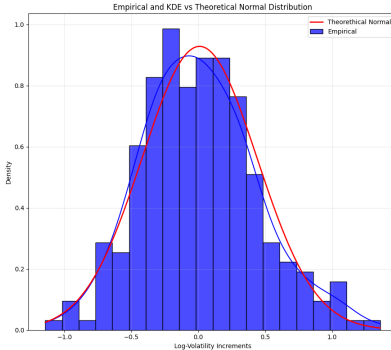


Figure 15: Log-Vol. increments.

Here we can observe the overlap between the empirical density (blue bins), the kernel density estimation based on the observations (blue line), and the theoretical Gaussian density (red line). The deviations from the theoretical curve are consistent with the finite sample size of the observations.

4.2 Parameters estimation.

4.2.1 \mathbb{P} vs \mathbb{Q} .

In models of rough stochastic volatility the Hurst exponent plays a central role in characterizing the roughness of volatility trajectories. Since the primary objective of the model is option pricing all parameters ultimately need to be specified under the risk-neutral measure \mathbb{Q} . However, while risk premia and drift-related quantities are measure-dependent and therefore must be calibrated directly under \mathbb{Q} , utilizing market data (IVS, option prices), the Hurst exponent is generally regarded as a structural property of the volatility process itself. For this reason, it is feasible to estimate the latter under the historical measure \mathbb{P} , from the time series of realized volatility, and to assume that this estimate remains valid under the risk-neutral one. In this work we propose this two-step approach: we first find H assuming it to be a structural characterization under \mathbb{P} and then we find the other parameters, fitting them under \mathbb{Q} . A more formal proof of this invariance ((inv.)) and in particular of the fact that the covariance function is the same in both measures, meaning that the covariance of increments (that determines the roughness or the smoothness) stays the same, when changing measure, is given in Appendix A.

4.2.2 H estimation.

When we estimate the Hurst exponent in the aim of this work what we are really doing is to find a quantitative measure for the roughness of volatility. The method proposed in [11] depends on the analysis of the log-volatility increments across different time resolutions and then assess their scaling behavior through statistical regressions. This approach allows us to find whether the process fluctuations are consistent with the standard diffusion models or if they are better represented by roughness, or smoothness, characteristic of fractional processes.

Define a discrete grid of observations of the volatility process (estimated as in Section 4.1), the mesh Δ that lies in $[0, T]$ partition our time series as: $\sigma_0, \sigma_\Delta, \dots, \sigma_{k\Delta}, \dots, \sigma_{T\Delta}$ for $k \in \mathbb{N}$. Set $N = \lfloor \frac{T}{\Delta} \rfloor$, for $p \geq 0$ we have:

$$m(p, \Delta) = \frac{1}{N} \sum_{k=1}^N |\ln(\sigma_{k\Delta}) - \ln(\sigma_{(k-1)\Delta})|^p$$

Then the main assumption made in [11] is that for some $s_p > 0$ and $b_p > 0$:

$$N^{ps_p} m(p, \Delta) \rightarrow b_p, \quad \text{as } \Delta \downarrow 0$$

Given some more technical conditions we can say that the volatility process belongs to the Besov smoothness space $\mathcal{B}_{p,\infty}^{s_p}$ and not to $\mathcal{B}_{p,\infty}^{s'_p}$ for $s'_p > s_p$. This implies that s_p can be seen as the regularity of the volatility when measured in the L_p norm sense. Functions that lie in that space are equipped with the Hölder property with parameter h , for any $h < s$. This means that if $\ln(\sigma_t)$ is a fBM with Hurst exponent H then, for any $p \geq 0$, the asymptotic above holds in probability with $s_p = H$.

Now, when we assume stationarity, the log-vol increments have the following fractal scaling property:

$$\mathbb{E}[|\ln(\sigma_\Delta) - \ln(\sigma_0)|^p] = A_p \Delta^{\psi_p}$$

where the expectation is our empirical estimate of $m(p, \Delta)$, A_p is a constant depending on p and $\psi_p = H \cdot p$. When we do log-log regression, we obtain:

$$\ln(\mathbb{E}[|\ln(\sigma_\Delta) - \ln(\sigma_0)|^p]) = \ln(A_p) + (H \cdot p) \ln(\Delta)$$

And finally, to get our estimate of H we just need to regress ψ_p against p and the slope will be our best fitting H .

The parameter p represents the order of the statistical moment considered in the scaling law. Empirically, small values of p (e.g. $p = 1$) capture typical or mean fluctuations, while larger values of p focus on rare, large deviations and therefore probe the intermittency or multifractality of the process. If the scaling exponent ψ_p depends linearly on p (for example, $\psi_p = c p$, as we will see, is the case), the process is said to be *monofractal*, implying that all moments scale in the same way. Conversely, a nonlinear dependence of ψ_p on p indicates *multifractality*, where different moments exhibit distinct scaling behaviors. Below we show the plot for the first regression, $\ln(\mathbb{E}[|\ln(\sigma_\Delta) - \ln(\sigma_0)|^p]) = \ln(A_p) + (H \cdot p) \ln(\Delta)$:

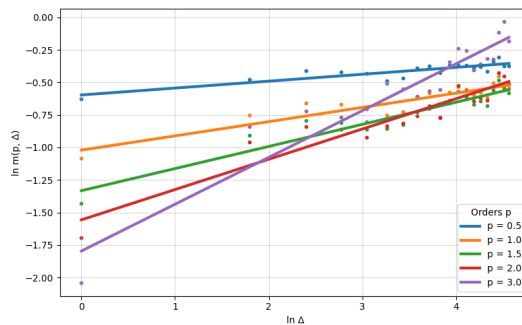


Figure 16: Regression of $\ln m(p, \Delta)$ against $\ln \Delta$.

From this we get our slope intercepts for various p and we simply need to regress again to get:

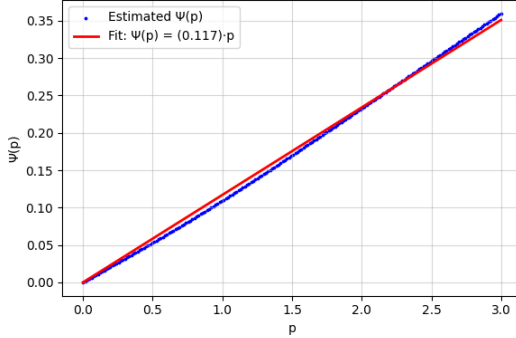


Figure 17: Regression of ψ_p against p .

This finally gives us the estimated $H \approx 0.117$. Or, equivalently, an α , defined as in Section 2.2, of $\alpha = H - \frac{1}{2} \approx 0.117 - 0.5 = -0.383$

4.2.3 Sanity check of the method.

To assess the finite-sample performance of the Hurst exponent estimator, a Monte Carlo study on a simple fractional process, $X_n = e^{W_n^H}$, was conducted for sample sizes $n = \{252, 504, 1008\}$, with the true Hurst exponent fixed at $H_{\text{true}} = 0.3$. Then for each n , $N_{\text{sim}} = 1000$ realizations of fractional Brownian motion were generated using the Davies–Harte method and the estimator \hat{H} was computed from the logarithm of the simulated process. The results are summarized in Table 3

Table 3: Monte Carlo Sanity Check for Hurst Exponent Estimation at Different Sample Sizes

Statistic	$n = 252$	$n = 504$	$n = 1008$
True Hurst exponent (H_{true})	0.3000	0.3000	0.3000
Mean estimated Hurst exponent	0.2643	0.2840	0.2916
Standard deviation of estimates	0.0999	0.0657	0.0468
Bias	-0.0357	-0.0160	-0.0084
Monte Carlo SE of the mean	0.00316	0.00208	0.00148
Approx. 3σ error bound	± 0.00948	± 0.00624	± 0.00444

As expected, the empirical mean $\mathbb{E}[\hat{H}]$ approaches H_{true} as n increases, indicating asymptotic unbiasedness. Interestingly, if we look at $\sigma_{\hat{H}}\sqrt{n}$, we obtain an approximately constant result ≈ 1.5 ; this implies that $\text{Var}_{\hat{H}} \propto n^{-1}$. This is consistent with the self-similarity properties of the fBM.

4.3 Other parameters.

The calibration of stochastic volatility models and, in particular, of our rough volatility specification implies that the loss function to be minimized, a Vega-weighted call-price squared difference with some arbitrage penalties, is highly nonlinear, nonconvex, and nondifferentiable.

This complexity arises from several structural features of the model: the volatility dynamics depend on convolutions and fractional kernels, introducing long-memory effects; the option pricing map involves exponentials and integrals of correlated stochastic processes and in the Monte Carlo setting, the objective function is subject to numerical noise. Consequently, classical local gradient-based algorithms (e.g., L-BFGS-B, SLSQP) often converge rapidly but are prone to becoming trapped in local minima and are sensitive to the choice of initial parameters. We can remedy this problem by using the Differential Evolution algorithm. This is first used to perform a global exploration of the parameter space, followed by a local refinement using a deterministic optimizer such as L-BFGS-B. Then a secondary application of the above two steps approach can be performed again by constructing the boundaries around the first found parameters. This strategy is known to work well, look for example at [19] and [20].

4.3.1 Differential Evolution algorithm.

Differential Evolution (DE) [21] is a stochastic, population-based optimization algorithm. In each iteration, every candidate solution in the population is mutated by combining it with other randomly selected candidates to generate a trial vector. Specifically, two distinct population members are randomly chosen, and their difference is used to perturb the best individual x_0 :

$$b' = x_0 + F(x_{r_0} - x_{r_1})$$

where F is the mutation scaling factor.

A trial vector is then constructed by recombining parameters from b' . Beginning from a randomly selected index i , parameters are sequentially (modulo-wise) filled from either b' or the original candidate. The selection is governed by a binomial process: for each parameter, a random number in $[0, 1)$ is drawn, if it is less than the recombination constant, the value from b' is used; otherwise, the value from the original candidate is retained. The final parameter is always taken from b' . Once the trial vector is formed, its fitness is evaluated. If the trial outperforms the original candidate, it replaces it in the population. Furthermore, if it surpasses the best-known solution, it also becomes the new best candidate.

Below we propose a visualization of the algorithm, applied to the Ackley function, which has a lot of steep ridges and local minima:

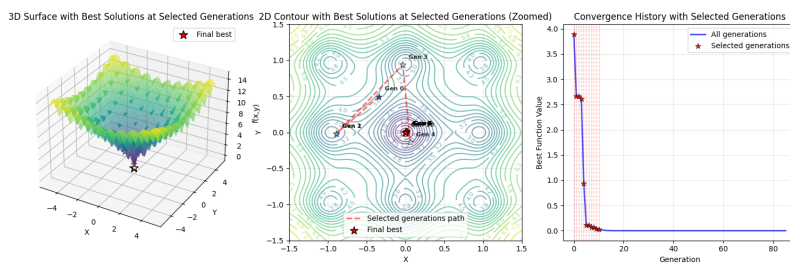


Figure 18: DE for various generations on the Ackley function.

It is clear that the DE algorithm's robust global search capability and population-based methodology enable it to produce very good optimization results on that function, even after a small number of

generations. DE successfully investigates the function's multidimensional landscape, which is characterized by its many local minima, by preserving a varied collection of candidate solutions. By encouraging exploration and avoiding premature convergence DE's mutation and crossover mechanisms help the population avoid falling into local traps. Consequently, DE maintains stability and robustness throughout the optimization process while quickly approaching the global optimum.

4.3.2 Loss and Objective functions.

The loss function was defined as:

$$L(\theta) = \frac{\sum_m v_m (C_m^{\text{model}} - C_m^{\text{market}})^2}{\sum_m v_m} \quad (6)$$

This is a Vega-weighted average squared error. We set m to be the node (T_i, K_j) , v_m the Vega value at that node and C_m the call price, the value surface for C_m was obtained by inverting the SVI surface from Section 3.2, utilising the Forward Black equation. The theoretical rationale behind this weighting is that for pricing we care the most about options that are in the ATM level, moreover if we think about it in an implied volatility perspective we deduce that the general level of the implied volatility surface is dictated by the ATM value, the numerical justification for using prices rather than volatilities is that out-of-the-money (OTM) volatilities are very small and thus susceptible to finite-precision errors. Prices provide more stable numerical behavior.

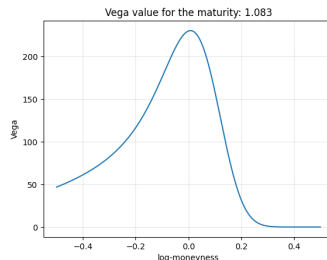


Figure 19: Vega plot for a call option with maturity ≈ 1 year.

The final objective function is then:

$$J(\theta) = L(\theta) + \lambda_i p_i$$

Where p_i are three different penalty functions that are weighted by a fixed λ_i , in particular those are:

- A penalty for the slope. This enforces monotonicity and acts by checking if the change of the call price with respect to the strike is effectively decreasing as the strike increases and bounding the derivative to be: $-D(T) \leq \frac{\partial C}{\partial K} < 0$. The upper bound is of easy intuition instead for the lower bound we can make the following argument: take two European call options with $K_1 < K_2$ their prices are $C(K_1)$ and $C(K_2)$ then we go long K_1 and short K_2 with a total cost of $\text{Cost} = C(K_1) - C(K_2)$ with maximum payoff $K_2 - K_1 = \Delta K$ if $S_T > K_2$ because this caps how much we can ever gain from this

spread, it also defines the constraint of how much we can pay for it, that is, never more than ΔK . This implies:

$$C(K_1) - C(K_2) \leq \Delta K D(T) = \frac{C(K_1) - C(K_2)}{\Delta K} \geq -D(T)$$

This yields for strikes K_1 and $K_2 = K_1 + \Delta K$, with ΔK small, that $\frac{\partial C}{\partial K} \geq -D(T)$

- A penalty to ensure no butterfly arbitrage. For a fixed maturity T the Call prices must be a convex function in the strike K . This means that the second discrete difference:

$$C(K_{j+1}) - 2C(K_j) + C(K_{j-1}) \geq 0$$

should hold true for all adjacent strikes. This holds for an equispaced strike grid, as in our case.

- The last one is a simple calendar penalty. In fact we know that for call options with no dividends and with non-negative interest rates, in order to avoid across maturities arbitrage we must have:

$$C(T_i, K_j) \geq C(T_{i-n}, K_j), \quad \forall n \in [1, 2, \dots, i]$$

4.4 Computational aspects.

4.4.1 RFSV.

To speed up the calibration it was needed to switch to a better computational routine than the one proposed in Section 2.2.5. The major improvements that were made concerned the computation of the Volterra convolution and the integration inside the kernel, the martingality check for this fast method is provided in Section 7.6. The Volterra convolution calculation was replaced using the following property of the Fourier transform:

$$\mathbf{F}\{f * \Delta W^{(2)}\} = \mathbf{F}\{f\} \cdot \mathbf{F}\{\Delta W^{(2)}\}$$

So basically, we just compute the (circular) convolution of the 2 Fourier transformed series and then we do:

$$\mathbf{F}^{-1}\{\mathbf{F}\{f\} \cdot \mathbf{F}\{\Delta W^{(2)}\}\}$$

to get our result back, the thing that was necessary also to do was to include a "zero-padding", this is because when we use the discrete Fourier transform to implement the above what we are really doing is a periodic convolution defined as:

$$c[i] = \sum_{m=0}^i a[i]b[(i-m) \bmod T] \text{ instead of } c[i] = \sum_{m=0}^i a[i-m]b[m] \quad (7)$$

the total length of the linear convolution is $2T - 1$, where T is the length of the time simulation we want. Obviously we truncate the convolution to keep only the values we are interested in, if we want the first t we truncate at the index $t - 1$ (0-indexed summation). For a small example look at 7.4. We need to

choose a padding length of at least $2T - 1$, and to leverage the properties of the Cooley-Tukey algorithm, that partition recursively by dividing by 2 the series, we choose it to be next power of 2 bigger than $2T - 1$.

Now, as for the integration inside the kernel 3, what we had was:

$$f(x) = \frac{\gamma}{\Gamma(1+\alpha)} (x^\alpha - k e^{-kx} \int_0^x e^{ku} u^\alpha du)$$

Now, set the integral we want to approximate to be:

$$I(x) = \int_0^x e^{ku} u^\alpha du$$

what we were originally doing was to call the function `scipy.quad` that performs quadrature by recursively evaluating the function at many points to check for integration error, we know that recursive call can be very heavy, in particular if the call stack becomes very tall. What it is to be realized is that the integration grid is uniform, we have in fact spacing of $j\Delta t$ with $j \in \mathbb{N}$, this means we can integrate incrementally, without the need to recompute the integral for each time step from the beginning, let $x_j = j\Delta t$; then:

$$I(x_j) = I(x_{j-1}) + \int_{x_{j-1}}^{x_j} e^{ku} u^\alpha du$$

and then the integral was solved with a fixed quadrature formula (Simpson's 1/3 rule):

$$\int_{x_{j-1}}^{x_j} q(u) du \approx \frac{\Delta t}{6} [q(x_{j-1}) + 4q(\frac{x_{j-1}+x_j}{2}) + q(x_j)]$$

in which $q(u) = e^{ku} u^\alpha$. To have a feel of the integration error of this method look at 7.5.

The third efficiency improvement was to simulate once and slice as much as needed, if we need to simulate for a set of maturities $[T_1, T_2, \dots, T_n]$ instead of simulating one time for each of them we just simulate until the longest maturity T_n and then slice the results to match the shorter ones.

The last improvement was to use antithetic variates inside the Monte Carlo simulations, for each generated random variable $Z \sim \mathcal{N}$ we also used, leveraging the symmetry of the Gaussian, $-Z$. By guaranteeing negatively correlated sample pairs this method successfully decreased the estimator's variance while maintaining objectivity. This increased the stability and effectiveness of the calibration procedure by enabling us to double the effective number of simulations without producing extra random numbers.

4.4.2 Heston.

To introduce the Heston model in an efficient, easy to calibrate manner we work with its analytical semi-closed form solution obtained by applying the Fourier (or integral) inversion theorem. This method permits the direct computation of European call option prices for arbitrary strikes and maturities, replacing the need to calculate such prices stochastically via time-consuming Monte Carlo simulations. Below

we give the closed form solution given in [9]:

$$C_T(k) = \frac{e^{-\alpha k}}{2\pi} \int_{-\infty}^{\infty} e^{-ivk} \psi_T(v) dv = \frac{e^{-\alpha k}}{\pi} \int_0^{\infty} e^{-ivk} \psi_T(v) dv$$

Above, the second equality holds because the integral is of an even function in its real part, i is the imaginary unit and the function inside is defined as:

$$\psi_T(v) = \frac{e^{-rT} \phi_T(v - (\alpha + 1)i)}{\alpha^2 + \alpha - v^2 + i(2\alpha + 1)v}$$

We need now to choose a good candidate for the characteristic function of the process (ϕ_t). We have a couple, but the final choice is the following, proposed by [22]:

$$\begin{aligned} \phi_T(u) = & \exp\{iu(\ln S_0 + (r - q)T)\} \cdot \exp\{\theta \kappa \xi^{-2}[(\kappa - \rho \xi iu - d)T - 2\ln(\frac{(1 - ge^{-dT})}{1 - g})]\} \cdot \\ & \cdot \exp\{v_0 \xi^{-2}(\kappa - \rho \xi iu - d) \frac{1 - e^{-dT}}{1 - ge^{dT}}\} \end{aligned}$$

where d and g are:

$$d = \sqrt{(\rho \xi iu - \kappa)^2 + \xi^2(iu + u^2)} \quad \text{and} \quad g = \frac{\kappa - \rho \xi iu - d}{\kappa - \rho \xi iu + d}$$

For a more precise reason, see 7.7.

4.5 Calibration routine.

We used the DE algorithm with 60 generations and 4,000 Monte Carlo simulation paths (net to the antithetic) to perform a rough global search in the initial step of the calibration procedure. This step aims to maintain computational efficiency by conducting a general exploration of the parameter space and identifying regions that might contain optimal solutions. It provided a useful starting point for the ensuing refinement stage. Building on the preliminary findings we increased the number of generations to 120 and the number of Monte Carlo paths to 10,000 in order to perform a more thorough and computationally demanding calibration. The optimization's accuracy and stability were greatly enhanced by this higher-resolution configuration, which made it possible for the DE algorithm to converge more precisely toward the global minimum.

On the other hand we employed the same DE framework for calibration of the Heston model as much as in terms of evolutionary parameters, same 60 and 120 generation settings for exploratory and refinement stages, respectively, but without Monte Carlo simulation. Since the Heston model enables an analytical solution to option pricing through the characteristic function and Fourier transform methodology no path generation using stochastic methods was required. This analysis-based formulation reduced computational cost and eliminated statistical noise inherent in Monte Carlo-based methods, resulting in faster convergence of the optimization. By these procedures the same methodological approach was preserved in both models and the computational strategy was adapted to the unique individual characteristics of each pricing environment.

5 Results.

We separated the available maturities into three distinct segments in order to examine the model's behavior over various time horizons. There were five maturities in the short-term segment, which ranged roughly from 0.72 to 2.16 years; four maturities in the medium-term segment, which ranged from 2.53 to 3.61 years; and three maturities in the out-of-sample (OOS) segment, which ranged from 3.97 to 6.17 years.

For the RFSV we simulated with the parameters found in the previous section using 300'000 Monte Carlo paths.

We assessed the model ability to capture short-lived volatility dynamics by optimizing and evaluating the model parameters solely using the short-term maturities for the short-term calibration. In a similar vein the medium-term maturities were used for both calibration and evaluation with an emphasis on the model's capacity to capture intermediate market structures.

To find the performance in the out-of-sample context we calibrated the model using all the maturities up to 3.61 years, those are the ones used in both short and medium term fitting. After the calibration we then evaluated the results in the remaining maturities, the ones from 3.97 to 6.17 years. This method provides a consistent procedure to assess the models' fit bucketed by maturity ranges as well as the predictive capacity that extends beyond the calibrated horizon.

Table 4: Maturity classification for calibration and out-of-sample analysis for the RFSV routine.

Category	Maturities for Calibration	Maturities for Evaluation
Short-term	0.7222, 1.0833, 1.4444, 1.8056, 2.1667	0.7222, 1.0833, 1.4444, 1.8056, 2.1667
Medium-term	2.5278, 2.8889, 3.2500, 3.6111	2.5278, 2.8889, 3.2500, 3.6111
Out-of-sample	0.7222, 1.0833, 1.4444, 1.8056, 2.1667, 2.5278, 2.8889, 3.2500, 3.6111	3.9722, 4.6944, 6.1667

For the Heston model we used a more straightforward calibration approach that was primarily intended to serve as a reference point for comparison rather than as the primary focus of the study. We used the maturities up to 3.61 years for a single calibration across the prices surface. This method was adequate for creating a trustworthy benchmark to assess the performance of the more intricate model created in this work and was computationally efficient.

Following the finding of the global calibration we assessed the Heston model using the same segmentation framework that was employed for the other analyses: the out-of-sample maturities (3.97–6.17 years), the medium-term maturities (2.53–3.61 years), and the short-term maturities (0.72–2.16 years). A comparison of outcomes across models and maturity ranges is made possible by this uniform evaluation framework.

Both models were calibrated according to their theoretical structure and typical best-practices: the

RSFV model was calibrated, in the short and medium-term cases, making use of maturities "clusters" to reflects its short-term memory dynamics. The Heston was fitted jointly, this is consistent with its Markovian structure and global parameterization. This approach ensure a fair comparison, in which each model is evaluated under its natural calibration framework. However, the out-of-sample procedure is exactly the same for both.

In addition to the segmentation by maturities, we further classified the data according to log-moneyness in order to evaluate model performance across different regions of the implied volatility surface.

- The at-the-money (ATM) region, defined by $|k| \leq 0.05$, includes options whose strikes are close to the current spot level up to the forward.
- The mid-moneyness (MID) region, defined by $0.05 < |k| \leq 0.15$, covers moderately in- and out-of-the-money options, where curvature and skew effects start to emerge.
- The WINGS region, defined by $|k| > 0.15$, corresponds to deep in- or out-of-the-money options, where option prices are more sensitive to the tails of the return distribution and the model's capacity to capture extreme events.

5.1 Evaluation metric.

To quantitatively assess the calibration and evaluation results, we employed the Mean Absolute Error (MAE) as the primary performance metric. It is defined as:

$$\text{MAE}_{t,j} = \frac{1}{N_{t,j}} \sum |x_{t,j}^{\text{model}} - x_{t,j}^{\text{market}}|$$

where the (t, j) index indicates the maturity (t) and the moneyness bucket (j) in which we are evaluating the metric (x), that could be either the implied volatility or the price.

For the Monte Carlo-based fit, where stochasticity introduces variability across runs, we repeated the evaluation 30 times and computed the average MAE over these realizations. To quantify the statistical uncertainty associated with this estimate, we constructed a confidence interval (CI) for the mean MAE using the Student's t -distribution:

$$\text{CI} = \pm t_{(1-\alpha/2, N-1)} \cdot \frac{s}{\sqrt{N}}$$

s is the sample standard deviation for the MAE observations in that bucket and maturity, $N = 30$ is the number of runs to create the confidence interval and $t_{(1-\alpha/2, N-1)}$ is the t -distribution with a confidence level of $(1 - \alpha)$ and $N - 1$ degrees of freedom.

Since the number of repeated runs in Monte Carlo-based fits is relatively small and the true population variance of the MAE is unknown, the Student- t was utilized to construct the confidence interval. The normal (Gaussian) approximation is not entirely suitable in these circumstances since it makes the assumptions that the sample size is big enough for the Central Limit Theorem to work and that the variability of the sample mean is perfectly known.

The uncertainty in estimating the population standard deviation from a finite sample, however, is explicitly taken into account by the t -distribution. Its shape is determined by the degrees of freedom ($v = N - 1$); as N increases, it converges to the normal distribution. We guarantee that the resulting confidence interval appropriately captures the sampling variability of the MAE as well as the finite number of calibration repetitions by employing the critical value $t_{(1-\alpha/2,N-1)}$. This gives a more conservative and statistically sound estimate of the model's performance uncertainty by making the interval marginally wider than one based on a Gaussian distribution.

Thus we obtain the final metric:

$$\text{MAE}_{t,j}^{\text{CI}} = \bar{\text{MAE}}_{t,j} \pm \text{CI}_{t,j}^{\alpha}$$

The above will be expressed in basis points (bp), that is the number multiplied by 10'000. For example, if we see a price MAE of 5'500 this indicates an average error of \$ 0.55.

5.2 Short-term fit.

Here we provide the MAE metrics in terms of the implied volatilities generated, in Section 13 we give the same analysis for the prices errors.

This section is devoted to the analysis of the models' performance over the short-term range of maturities, those are the ones from roughly 0.72 to 2.16 years. The behavior of the short-lived options, which are usually more impacted by volatile market dynamics and sharp volatility swings, is well represented in this segment. When we look at the fit in this region we can determine how well the model captures the implied volatility short term structure and the level of sensitivity to high-frequency market fluctuations.

Below we provide the table for the implied volatility valuation, both for the RFSV:

Table 5: RFSV MAE by Moneyness Bucket - Implied Volatility (in bps)

Maturity	ATM	MID	WINGS	Overall
0.72	$25.102 \pm 0.277(0.373)$	$80.333 \pm 1.001(1.349)$	$146.109 \pm 1.753(2.362)$	$193.729 \pm 2.082(2.806)$
1.08	$31.718 \pm 0.388(0.524)$	$31.400 \pm 0.347(0.468)$	$101.395 \pm 1.230(1.658)$	$189.103 \pm 2.172(2.927)$
1.44	$13.563 \pm 0.160(0.216)$	$29.478 \pm 0.351(0.474)$	$67.253 \pm 0.853(1.150)$	$103.830 \pm 1.132(1.526)$
1.81	$15.668 \pm 0.182(0.246)$	$24.546 \pm 0.281(0.379)$	$51.543 \pm 0.577(0.778)$	$103.161 \pm 1.181(1.591)$
2.17	$24.386 \pm 0.295(0.398)$	$16.071 \pm 0.167(0.226)$	$61.385 \pm 0.681(0.917)$	$101.702 \pm 1.398(1.884)$
Overall	$22.163 \pm 0.246(0.331)$	$36.444 \pm 0.383(0.516)$	$84.745 \pm 1.019(1.373)$	$139.356 \pm 1.735(2.338)$

Note: Values are Mean Absolute Error (MAE) \pm 95% CI (99% CI).

And the same for the Heston:

Table 6: Heston Model MAE by Moneyness Bucket (in bps)

Maturity	ATM	MID	WINGS	Overall
0.72	75.740	60.345	147.969	194.018
1.08	23.456	53.615	140.561	213.184
1.44	20.786	25.084	61.998	110.874
1.81	35.092	41.317	42.560	108.302
2.17	11.305	17.347	51.222	103.782
Overall	33.276	39.542	88.862	146.032

That gives us an improvement:

Table 7: MAE Improvement (Heston – RFSV) in bps

Metric	ATM	MID	WINGS	Overall
Improvement (Δ MAE)	11.113 (33.396%)	3.098 (7.835%)	4.117 (4.633%)	6.676 (4.572%)

The RFSV model outperformed the Heston benchmark, as demonstrated by the results for the short-term maturities. It consistently improves across all moneyness buckets, as Table 7 demonstrates. The biggest gain is seen in the at-the-money (ATM) region, where the mean absolute error drops by about 11.1 bps in comparison to the Heston model. This notable improvement suggests that the short-term volatility dynamics surrounding the strike level that are most susceptible to market expectations are better captured by the rough framework. Our model offers a more adaptable and reliable fit across the whole volatility surface, as evidenced by the improvements that are still positive in the wings and mid-moneyness regions, by roughly 4.1 and 3.1 bps, respectively.

Below we give the plot for the implied volatilities comparison:

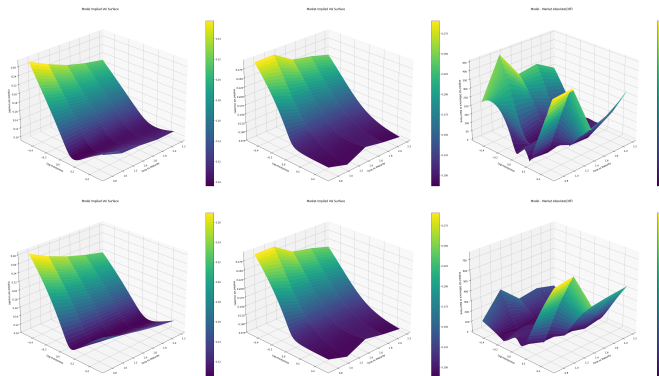


Figure 20: Comparison of the two generated implied vol surfaces with the market, and their errors, on the short-term maturities. RFSV above, Heston below.

5.3 Medium-term fit.

The performance over the medium-term region, roughly between 2.53 and 3.61 years, are assessed in the following. In this expirations range, which acts as a transitional area from the short-term market dynamics to the longer-term structural behavior, the pricing is influenced by both short-lived shocks and lasting factors. This section's analysis of the fitting power, allows us to evaluate the calibration accuracies and stabilities beyond the near horizon, by judging the optimization goodness with respect to the evolution of the volatility surface as the time to maturity increases.

Table 8: RFSV MAE by Moneyness Bucket - Implied Volatility (in bps) - Medium Term

Maturity	ATM	MID	WINGS	Overall
2.53	$8.106 \pm 0.091(0.122)$	$25.831 \pm 0.316(0.426)$	$19.571 \pm 0.244(0.329)$	$54.123 \pm 0.569(0.767)$
2.89	$19.473 \pm 0.238(0.321)$	$22.990 \pm 0.271(0.366)$	$25.373 \pm 0.280(0.378)$	$50.982 \pm 0.612(0.824)$
3.25	$32.742 \pm 0.381(0.514)$	$28.816 \pm 0.336(0.452)$	$31.819 \pm 0.379(0.511)$	$50.992 \pm 0.619(0.834)$
3.61	$48.712 \pm 0.518(0.699)$	$44.088 \pm 0.534(0.719)$	$42.078 \pm 0.482(0.650)$	$55.779 \pm 0.708(0.954)$
Overall	$26.736 \pm 0.295(0.397)$	$30.391 \pm 0.337(0.454)$	$29.841 \pm 0.311(0.419)$	$52.781 \pm 0.591(0.797)$

Note: Values are Mean Absolute Error (MAE) \pm 95% CI (99% CI).

The benchmark table:

Table 9: Heston Model MAE by Moneyness Bucket (in bps) - Medium Term

Maturity	ATM	MID	WINGS	Overall
2.53	5.395	12.365	52.892	100.452
2.89	10.294	13.825	48.931	93.345
3.25	18.492	20.174	45.041	86.686
3.61	29.921	30.322	45.895	83.598
Overall	16.025	19.171	48.190	91.020

With the differential:

Table 10: MAE Improvement (Heston – RFSV) in bps - Medium Term

Metric	ATM	MID	WINGS	Overall
Improvement (Δ MAE)	$-10.711 (-66.839\%)$	$-11.220 (-58.525\%)$	$18.349 (38.076\%)$	$38.239 (42.012\%)$

Note: A negative value indicates the RFSV MAE is greater than the Heston MAE.

A more nuanced comparison between the RFSV and Heston models is shown by the results for the medium-term maturities. The Heston model performs better than the RFSV in the at-the-money (ATM) and mid-moneyness (MID) regions, where the RFSV produces higher mean absolute errors by

roughly 10.7 bps and 11.2 bps, respectively, as Table 10 illustrates. The medium-term horizon’s generally smoother and more persistent volatility dynamics are responsible for this behavior. The classical stochastic volatility formulation of the Heston model, which is characterized by a single mean-reverting variance process, is still adaptable enough to account for the curvature of the implied volatility surface close to the central strikes in such circumstances. Because of this its extra complexity might not offer significant advantages in these smoother areas and maturities, sometimes resulting in less effective fits.

Nevertheless, the RFSV model shows clear improvements in the wings, achieving an average gain of about 18.3 bps relative to the Heston model. In contrast to the Heston framework, which tends to underestimate curvature and tail behavior, the rough volatility structure improves the model’s ability to replicate the implied volatility surface’s steeper skews and fatter tails. The overall improvement of 38.2 basis points demonstrates that the RFSV model offers a more accurate and adaptable depiction of volatility behavior in the most extreme areas of the surface, even though the Heston model is still competitive around central moneyness levels for medium maturities.

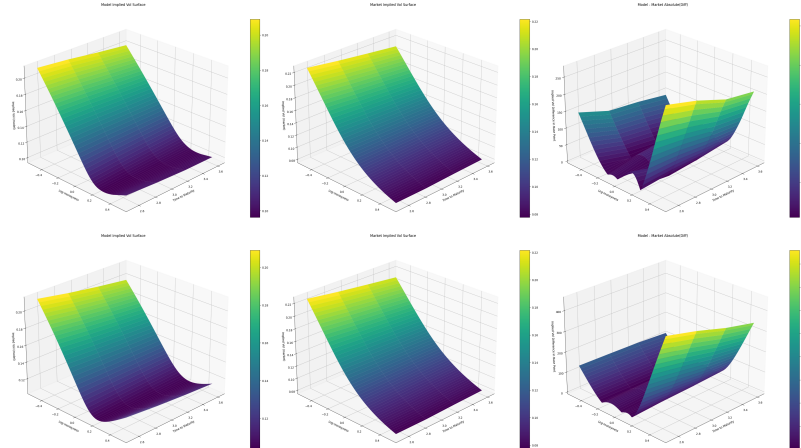


Figure 21: Comparison of the two generated implied vol surfaces with the market, and their errors, on the medium-term maturities. RFSV above, Heston below.

5.4 Out of sample fit.

Here we assess the models’ out-of-sample (OOS) performance, concentrating on maturities between roughly 3.97 and 6.17 years. In contrast to earlier analyses these maturities were not included in the calibration procedure, enabling a true evaluation of each model’s robustness and predictive power outside of the fitted data range. This discussion offers a critical test for the generalization of the models; a strong OOS performance shows that the framework captures the underlying volatility process instead of overfitting the data used in the calibration. We can see how well the RFSV and the Heston models extrapolate to the volatility surface structure to longer temporal terms and less constrained parts of the option space by analyzing the out-of-sample results over different moneyness buckets.

Table 11: RFSV MAE by Moneyness Bucket - Implied Volatility (in bps) - Out-of-Sample

Maturity	ATM	MID	WINGS	Overall
3.97	$23.386 \pm 0.204(0.276)$	$14.666 \pm 0.164(0.222)$	$23.992 \pm 0.265(0.357)$	$48.705 \pm 0.589(0.794)$
4.69	$37.289 \pm 0.459(0.619)$	$29.251 \pm 0.357(0.482)$	$15.091 \pm 0.185(0.249)$	$39.401 \pm 0.437(0.589)$
6.17	$64.839 \pm 0.735(0.991)$	$58.596 \pm 0.682(0.919)$	$33.515 \pm 0.396(0.533)$	$48.708 \pm 0.607(0.818)$
Overall	$42.058 \pm 0.463(0.623)$	$34.359 \pm 0.366(0.493)$	$24.443 \pm 0.285(0.384)$	$45.606 \pm 0.504(0.679)$

Note: Values are Mean Absolute Error (MAE) \pm 95% CI (99% CI).

Heston:

Table 12: Heston Model MAE by Moneyness Bucket (in bps) - Out-of-Sample

Maturity	ATM	MID	WINGS	Overall
3.97	42.564	42.429	54.305	88.591
4.69	56.760	55.222	56.386	82.065
6.17	81.881	79.160	71.498	86.463
Overall	60.402	58.937	60.730	85.706

Improvements:

Table 13: MAE Improvement (Heston – RFSV) in bps - Out-of-Sample

Metric	ATM	MID	WINGS	Overall
Improvement (Δ MAE)	18.344 (30.370%)	24.578 (41.702%)	36.287 (59.751%)	40.100 (46.788%)

Note: A positive value indicates the RFSV MAE is lower than the Heston MAE.

The out-of-sample results noticeably show how the RFSV model performs better, in the generalization, than the Heston model. All the moneyness regions are consistently and significantly improved by the RFSV, we can see that in Table 13. The at-the-money (ATM) moneyness saw a reduction of about 18.3 basis points, the mid-moneyness was 24.6 bps better and the wings were superior by an impressive 36.3 basis points. These findings demonstrate that the RFSV model is far better than the benchmark when it is applied to maturities that are excluded from the calibration, in fact it retains a higher predictive power in addition to the successful fitting of the data for the in sample evaluation.

The notable improvements over the wings moneyness region show the value of our rough volatility framework, this captures the long lasting and fine-scale irregularities of the volatility process, those are not modeled by the smoother and non-rough Heston formulation. The overall enhancement of more than 40 bps in MAE shows that the RFSV model gives a more precise and plastic representation of the volatility surface, in particular for the sections outside the calibration scope. This remarkable characteristic demonstrates the RFSV model robustness and transferability as an empirically consistent description of market volatility behaviors.

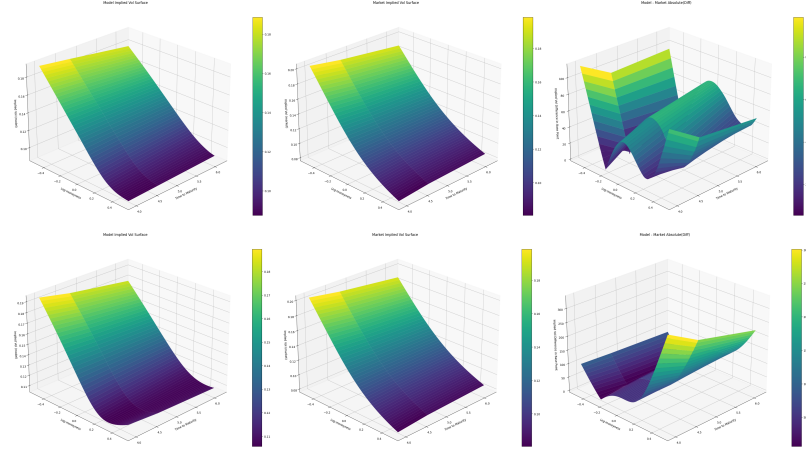


Figure 22: Comparison of the two generated implied vol surfaces with the market, and their errors, on the out-of-samples maturities.

5.5 Surmise.

A thorough comparison between the rough volatility model and the Heston benchmark has been provided by the analysis carried out across the short, medium and out-of-sample maturities. According to the results the RFSV framework clearly improves short-term maturities. Its capacity to capture high-frequency, rough volatility fluctuations results in significantly lower mean absolute errors, especially in the at-the-money region. The Heston model performs marginally better in the central moneyness buckets for medium-term maturities, indicating that it is appropriate for more stable and smooth volatility regimes. The Heston model tends to underestimate the implied volatility surface's curvature and asymmetry, whereas the RFSV model still performs better in the wings and the overall fit. The RFSV model's resilience and capacity for generalization are further supported by the out-of-sample analysis. The RFSV consistently achieves lower errors across all moneyness segments, when tested on maturities that were not part of the calibration. This confirms that the fundamental dynamics of market volatility beyond the fitted range are captured by its rough fractional structure. In contrast to traditional stochastic volatility models the RFSV model provides a more flexible and realistic depiction of the implied volatility surface. These results demonstrate the model's ability to replicate both short-term irregularities and long-term persistence of volatility. In Section 11 we plot the risk-neutral density plot to check if the volatilities generated are free of arbitrage.

5.6 Application.

In this section, two call option types: an Asian call option and a floating Lookback call option, are priced using the calibrated RFSV model.

The Asian call option introduces path dependence, since it has a payoff coming from the time-averaging of the underlying trajectory, enabling an evaluation of how well the model handles temporal dynamics. Secondly, the model's capacity to accommodate extreme value behavior in the simulated price

path is demonstrated by the floating Lookback call option, whose payout is contingent upon the smallest asset price recorded during the option's lifetime.

We will assume the maturity of our options is 2 years, a maturity not present in our original universe. We will use 500'000 MC paths and we will report the price with the standard error defined as: $3 \cdot (SD)/\sqrt{500000}$.

5.6.1 The Asian option.

An Asian option is characterized by the following payoff:

$$\mathcal{A} = (\frac{1}{T} \int_0^T S_u du - k)^+$$

Then the price is simply the discounted expectation of the payoff:

$$\Pi(\mathcal{A}, T) = e^{-rT} \mathbb{E}[\mathcal{A}]$$

To obtain \mathcal{A} , which is the time average of the underlying path, we can discretize the integral as:

$$\begin{aligned} \frac{1}{N\Delta t} \sum_{n=0}^{N-1} \int_{t_n}^{t_{n+1}} S_u du &\approx \frac{1}{N\Delta t} \sum_{n=0}^{N-1} \frac{S_{n+1} - S_n}{2} \Delta t = \\ &= \frac{1}{N} [\frac{S_0}{2} + \sum_{n=1}^{N-1} S_n + \frac{S_N}{2}] \end{aligned}$$

This yields the trapezoidal approximation for the Asian payoff:

$$\mathcal{A} \approx (\frac{1}{N} [\frac{S_0 + S_N}{2} + \sum_{n=1}^{N-1} S_n] - k)^+$$

5.6.2 The Lookback option.

The Lookback option has the following payoff:

$$\mathcal{L} = S_T - \min_{0 \leq t \leq T} S_t$$

Here, the payoff cannot be negative, by construction, so we drop the "positive-part" function, and then the price is:

$$\Pi(\mathcal{L}, T) = e^{-rT} \mathbb{E}[\mathcal{L}]$$

5.6.3 Pricing.

After simulating the MC paths for the maturity of 2 years using our calibrated RFSV parameters in the short-term case and setting a strike of $k = 550$, in the ATM region, we obtain the following prices:

Table 14: Comparison of Option Prices with Standard Errors

Option Type	Price ± SE
Asian Price	33.53451 ± 0.14085
Lookback Price	98.62469 ± 0.25219

6 Conclusion.

This study has presented a comprehensive framework for modeling and calibrating volatility dynamics through the lens of fractional processes. Building upon the theoretical foundation introduced in Section 1, where the construction, main characteristics, and statistical properties of the fractional Brownian motion were discussed; the proposed approach leverages the roughness inherent in financial volatility to enhance short-term forecasting accuracy and capture persistent market features.

Following the Rough Fractional Stochastic Volatility model definition in Section 2 and the introduction of the Heston model, which served as a comparison for the performance of the RFSV, the statistical description of the dataset and the development of a clear calibration objective function is made in Section 3. The estimation methods, discussed in Section 4, introduced a two-measure estimation approach. This approach separates the identification of the Hurst parameter under the physical measure \mathbb{P} from the calibration of the other parameters under the risk-neutral measure \mathbb{Q} for pricing.

The analysis and calibration results, summarized in Section 5, show that the RFSV model performs better in short-term maturities. It effectively captures the high-frequency, rough dynamics of volatility, resulting in much lower mean absolute errors, particularly in the at-the-money region. The Heston model still works well for smoother, medium-term volatility, showing slightly better performance in central moneyness buckets. However, the RFSV model offers a more accurate and flexible fit overall, especially in the wings where curvature and asymmetry matter.

Out-of-sample validation supports the strength and adaptability of the RFSV model. When tested on maturities not used in calibration, the RFSV consistently produces lower pricing and volatility errors across all moneyness segments. This shows that the model's fractional structure captures important features of market volatility beyond the fitted range, maintaining both rough short-term fluctuations and long-term memory.

At the conclusion of Section 5, we have shown how our model can be applied to the valuation of exotic or non-standard options written on a specific underlying asset. In particular we show how the flexibility of the Monte Carlo simulation method in managing intricate payoff structures and path-dependent features can be used to efficiently estimate the prices of such options. These examples demonstrate how flexible our framework is in capturing the unique features of exotic options and the usefulness of the MC approach in assessing instruments without closed-form analytical pricing formulas.

In summary this work highlights the effectiveness of the RFSV model for capturing the intricate dynamics of financial markets. By combining rigorous theoretical foundations with robust calibration techniques and practical pricing applications, the study demonstrates that accounting for volatility roughness substantially improves model realism and accuracy. The two-measure approach, which estimates the Hurst parameter under the physical measure \mathbb{P} and calibrates the remaining parameters under the risk-neutral measure \mathbb{Q} , proved to be both coherent and efficient. It allows for a clear separation between statistical estimation, which is fast and computationally inexpensive, and market calibration, which is slower but necessary, to get the risk-neutral parameters. Moreover, the successful application of the RFSV framework to the pricing of exotic options further emphasizes its adaptability and computational efficiency, reinforcing its value as a comprehensive and realistic tool for volatility modeling and derivative valuation.

7 Appendix A.

7.1 Proof of (1).

Take the Mandelbrot van Ness kernel:

$$g_t(u) = [(t-u)_+^{H-1/2} - (-u)_+^{H-1/2}]$$

Since this is deterministic and $g_t(u) \in L^2(\mathbb{R})$ we can apply Itô's isometry: $\mathbb{E}[(\int_{\mathbb{R}} f(u) dB_u)(\int_{\mathbb{R}} h(v) dB_v)] = \int_{\mathbb{R}} f(u)h(u) du$. Then take the integral representation of the fBM with the MvN kernel, ignore the normalization a_H , which is always positive:

$$W_t^H = \int_{\mathbb{R}} g_t(u) dW_u$$

Note how $\gamma_{W^H}(s,t) = \mathbb{E}[(\int_{\mathbb{R}} g_t(u) dW_u)(\int_{\mathbb{R}} g_s(v) dW_v)] = \int_{\mathbb{R}} g_t(u)g_s(u) du = \langle g_t; g_s \rangle$. Apply this form to the covariance function:

$$\sum_{i=1}^n \sum_{j=1}^n x_i x_j \gamma_{W^H}(t_i, t_j) = \sum_{i=1}^n \sum_{j=1}^n x_i x_j \langle g_{t_i}; g_{t_j} \rangle = \left\langle \sum_{i=1}^n x_i g_{t_i}; \sum_{j=1}^n x_j g_{t_j} \right\rangle = \left\| \sum_{i=1}^n x_i g_{t_i} \right\|_{L^2}^2 \geq 0$$

This prove that Σ is positive semi-definite.

7.2 Proof of (4)

The proof is given in discrete time:

$$\begin{aligned} E[S_k | \mathcal{F}_{k-1}] &= S_{k-1} E[\exp \{ \sigma_{k-1} \Delta W_k - \frac{1}{2} \sigma_{k-1}^2 \Delta t | \mathcal{F}_{k-1} \}] = \\ &= S_{k-1} \exp \{ -\frac{1}{2} \sigma_{k-1}^2 \Delta t \} E[\exp \{ \sigma_{k-1} \Delta W_k \} | \mathcal{F}_{k-1}] = \\ &= S_{k-1} \exp \{ -\frac{1}{2} \sigma_{k-1}^2 \Delta t \} \exp \{ \Delta t \frac{\sigma_{k-1}^2}{2} \} = S_{k-1} \end{aligned}$$

7.3 Proof of (inv).

To prove our claim that H is invariant under the change of measure. Express $(W_t^H)^{\mathbb{P}}$ as the integral of a deterministic kernel $g_t(u)$:

$$\int_0^t g_t(u) dW_u$$

Under \mathbb{P} we recover the usual $\gamma_{W^H}(s,t) = \frac{1}{2}(t^{2H} + s^{2H} - |t-s|^{2H})$ Now introduce θ_t , a (\mathcal{F}_t) -deterministic and square integrable process that respects Novikov. Then the exponential:

$$\lambda_T = \exp \left\{ \int_0^T \theta_s dW_s - \frac{1}{2} \int_0^T \theta_s^2 ds \right\}$$

defines an equivalent measure on \mathbb{Q} on the filtration, with $\lambda_T = \frac{d\mathbb{Q}}{d\mathbb{P}}$, thus by Girsanov:

$$\tilde{W}_t := W_t - \int_0^t \theta_s ds$$

is a Wiener process under \mathbb{Q} . Finally, express the fBM under the new measure:

$$W_t^H = \int_0^t g_t(u) dW_u = \int_0^t g_t(u) d\tilde{W}_u + m_t, \quad m_t := \int_0^t g_t(u) \theta_u du$$

crucially, this does not change the covariance, since we simply add a deterministic (given θ_t) shift m_t . This implies that, $\forall 0 \leq s < t$ and $0 \leq v < u$:

$$\text{Cov}_{\mathbb{Q}}[(W_t^H - W_s^H)(W_u^H - W_v^H)] = \text{Cov}_{\mathbb{P}}[(W_t^H - W_s^H)(W_u^H - W_v^H)]$$

Thus keeping the roughness/smoothness embedded by H the same.

7.4 Circular convolution example.

Take $a = [a_0, a_1, a_2]$ and $b = [b_0, b_1, b_2]$, then we have the linear convolution with the terms:

$$[c_0, c_1, c_2, c_3, c_4]^{\text{linear}} = [a_0b_0, a_0b_1 + a_1b_0, a_0b_2 + a_1b_1 + a_2b_0, a_1b_2 + a_2b_1, a_2b_2]$$

Now the circular convolution with no padding, periodic with period 3:

$$[c_0, c_1, c_2]^{\text{no pad}} = [a_0b_0 + a_1b_2 + a_2b_1, a_0b_1 + a_1b_0 + a_2b_2, a_0b_2 + a_1b_1 + a_2b_0]$$

With padding we add some 0's to a and b to make the total length at least $2T - 1 = 5$ so we have $a = [a_0, a_1, a_2, 0, 0]$, $b = [b_0, b_1, b_2, 0, 0]$ and we get:

$$[c_0, c_1, c_2, c_3, c_4]^{\text{pad}} = [a_0b_0, a_0b_1 + a_1b_0, a_0b_2 + a_1b_1 + a_2b_0, a_1b_2 + a_2b_1, a_2b_2]$$

this is exactly the linear convolution we want.

7.5 1/3 Simpson's rule error.

We know from [23], (5.1.15) that the error for the Simpson's one-third rule is the following:

$$-\frac{(x_j - x_{j-1})^5}{2880} q^{(4)}(n)$$

where $q^{(4)}$ is the fourth derivative w.r.t the integrand that is evaluated at some point n between x_j and x_{j-1} . Thus we obtain a relative absolute error, if we take a realistic k coming from the calibration, of $RAE \approx 0.075 \%$.

7.6 Martingality check for the fast method.

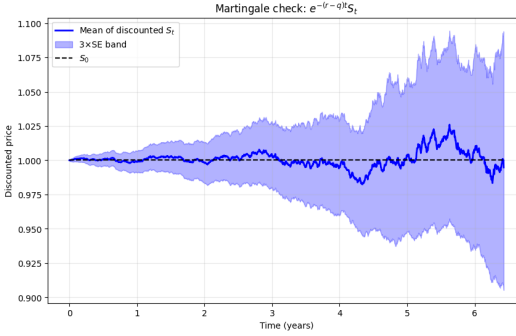


Figure 23: Here we plot the Martingality check for the "fast" scheme, since the parameters are the same as the "slow" Martingality check, we can see the integration scheme gave the same result, up to the MC error.

Moreover, below we show the time complexity improvement, w.r.t. the number of MC paths, between the two implementations.

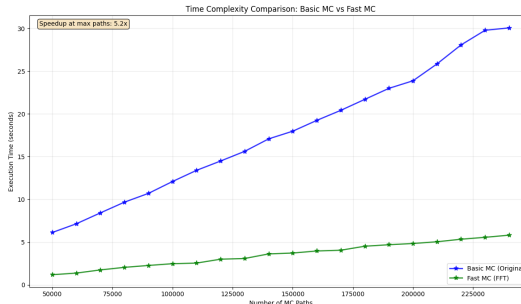


Figure 24: Time complexity comparison.

7.7 Heston CF choice.

As we know from [24] the literature proposes two different characteristic functions for the Heston process. The first, was the original one, proposed in [9]:

$$\begin{aligned}\phi_T^{(a)}(u) = & \exp\{iu(\ln S_0 + (r - q)T)\} \cdot \exp\{\theta \kappa \xi^{-2}[(\kappa - \rho \xi iu + d)T - 2 \ln(\frac{1 - g_1 e^{dT}}{1 - g_1})]\} \cdot \\ & \cdot \exp\{v_0 \xi^{-2}(\kappa - \rho \xi iu + d) \frac{1 - e^{dT}}{1 - g_1 e^{dT}}\}\end{aligned}$$

with:

$$d = \sqrt{(\rho \xi iu - \kappa)^2 + \xi^2(iu + u^2)} \quad \text{and} \quad g_1 = \frac{\kappa - \rho \xi iu + d}{\kappa - \rho \xi iu - d}$$

The other, proposed in [22]:

$$\begin{aligned}\phi_T^{(b)}(u) = & \exp\{iu(\ln S_0 + (r-q)T)\} \cdot \exp\{\theta \kappa \xi^{-2}[(\kappa - \rho \xi iu - d)T - 2 \ln(\frac{(1-g_2 e^{-dT})}{1-g_2})]\} \cdot \\ & \cdot \exp\{v_0 \xi^{-2}(\kappa - \rho \xi iu - d) \frac{1-e^{-dT}}{1-g_2 e^{dT}}\}\end{aligned}$$

where d and g_2 are:

$$g_2 = \frac{\kappa - \rho \xi iu - d}{\kappa - \rho \xi iu + d} = \frac{1}{g_1}$$

it has been reported, for example in [25], that the use of $\phi^{(a)}$ is associated with mispricing in vanilla options, due to numerical errors arising from the branch cut coming from the complex square root. This is evident when we plot the real part of both functions:

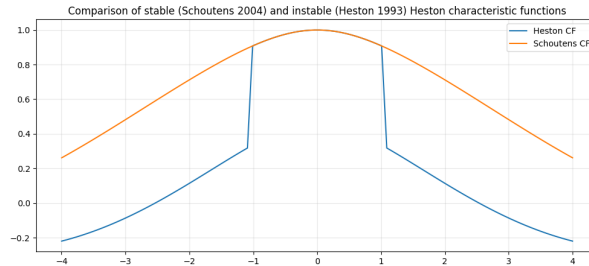


Figure 25: The real part of the two ϕ , with the estimated parameters and for the maximum maturity in our options chain, where the branch cut is evident.

8 Appendix B: Individual SVI smiles.

For the sake of completeness, below we also include the plot for the individuals smiles fitted with the SVI.

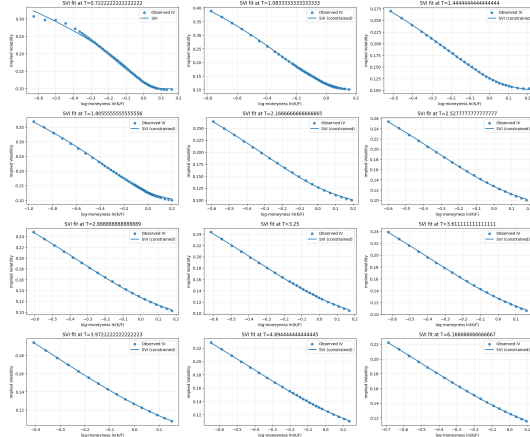


Figure 26: The fitted smiles arising from the SVI fitting.

9 Appendix C: Estimated parameters for RFSV.

In this section we report the parameters estimated under the \mathbb{Q} measure for the RFSV model. Those are split into the three terms we used for calibration. The last table is the output of the DE algorithm, where we report some insightful data.

Table 15: Short-term calibration parameters

Parameter	Value
$\ln \sigma_0$	-2.5921156107558887
ρ	-0.6517807885416091
k	0.6164834465809215
γ	0.8232134210271708

Table 16: Medium-term calibration parameters

Parameter	Value
$\ln \sigma_0$	-2.640702606113612
ρ	-0.7183368501523021
k	0.30923060849012657
γ	0.7909246322102209

Table 17: Whole-surface calibration parameters

Parameter	Value
$\ln \sigma_0$	-2.3502778575398926
ρ	-0.786254291033244
k	0.12751289549705747
γ	0.5330135895361081

Table 18: Differential Evolution (DE) Optimization Results for RFSV Model

Model Type	Completion Time (s)	Function Evaluations	Final Objective
RFSV ST	6667.4	15658	0.58084032
RFSV MT	8929.2	15608	0.50142916
RFSV OOS	4488.8	19468	1.07885225

10 Appendix D: Heston parameters.

Here we give the Heston parameters, estimated under the risk-neutral measure and calibrated on the short and medium-term maturities. We use this Heston model to benchmark the RFSV.

Table 19: Heston model global parameters

Parameter	Value
v_0	0.023989573784346168
κ	1.4898580170667166
θ	0.023409572433719
ξ	0.6449128872945478
ρ	-0.6112140498206449

Table 20: Differential Evolution (DE) Optimization Results for Heston Model

Model Type	Completion Time (s)	Function Evaluations	Final Objective
Heston	4760.5	8904	0.56990997

11 Appendix E: RND check of the calibrated IVS.

In this appendix we report the plots to check the absence of arbitrage of the generated implied volatility smiles in the RFSV case, those are found thanks to the formula of Gatheral to check for the butterfly spreads and the plot of the total implied variance to check for calendar spreads.

11.1 RFSV RND.

11.1.1 Short-term.

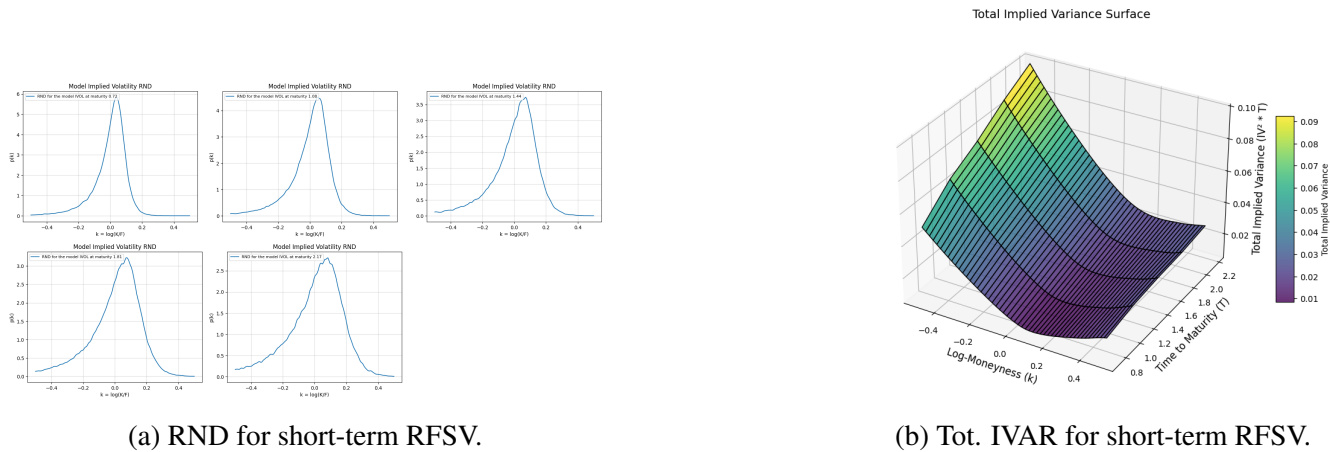


Figure 27: Absence of arbitrage check for the generated surface.

11.1.2 Medium-term.

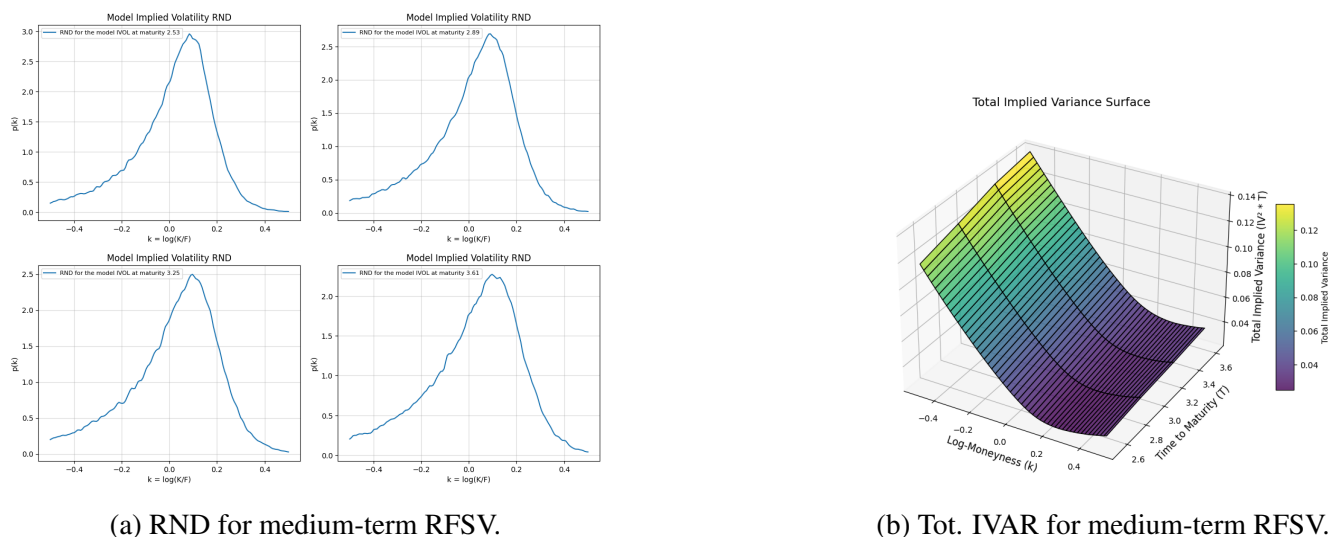


Figure 28: Absence of arbitrage check for the generated surface.

11.1.3 OOS.

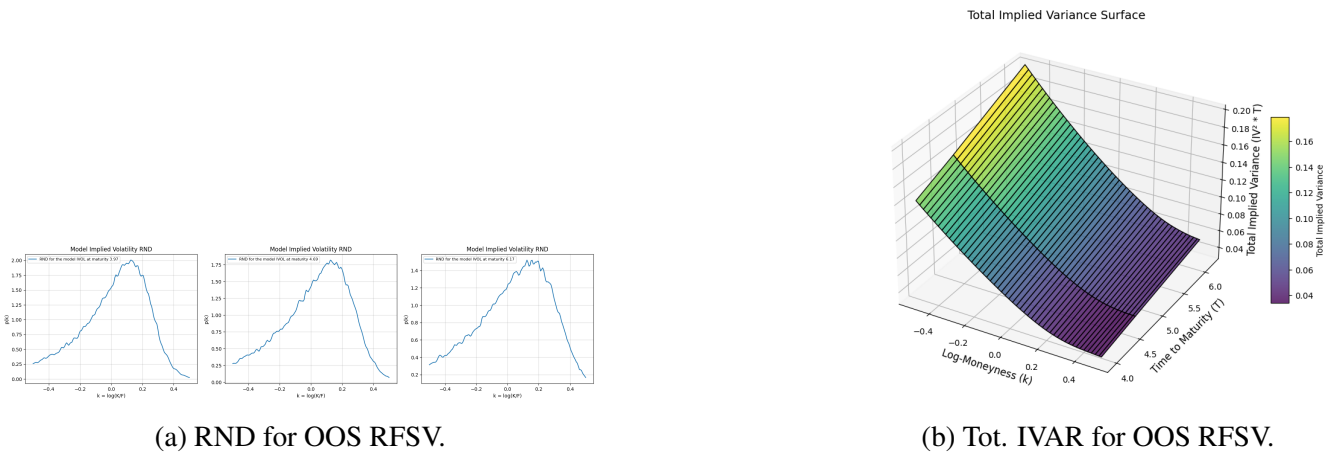


Figure 29: Absence of arbitrage check for the generated surface.

12 Appendix F: Heston RND.

In this appendix we report the plots to check the absence of arbitrage of the generated implied volatilities smiles in the Heston case, those are found thanks to the formula of Gatheral to check for the butterfly spreads and the plot of the total implied variance to check for calendar spreads.

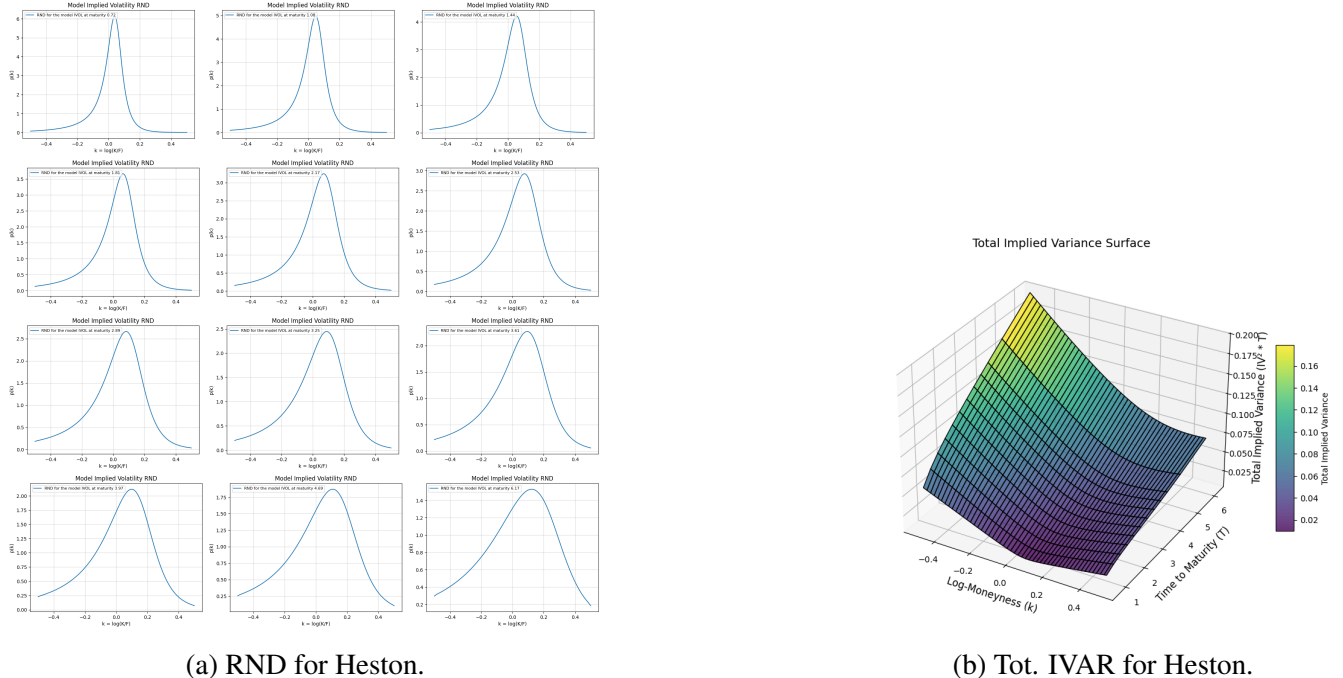


Figure 30: Absence of arbitrage check for the generated surface.

13 Appendix G: Prices MAE comparison.

13.1 Short-term.

Table 21: MAE by Moneyness Bucket - Prices (Short Term)

Maturity	ATM	MID	WINGS	Overall
0.72	4569.562 ± 52.818(71.184)	9598.026 ± 116.915(157.568)	7638.641 ± 90.123(121.461)	6249.688 ± 70.865(95.506)
1.08	7192.249 ± 76.486(103.082)	5198.760 ± 63.447(85.509)	6025.339 ± 77.606(104.591)	7260.872 ± 79.846(107.610)
1.44	3530.521 ± 34.653(46.703)	6005.155 ± 68.502(92.321)	7757.745 ± 100.328(135.213)	7416.571 ± 83.148(112.060)
1.81	4595.048 ± 50.431(67.966)	5926.363 ± 75.295(101.476)	7142.074 ± 78.608(105.941)	8480.322 ± 103.600(139.623)
2.17	7735.454 ± 82.983(111.838)	4496.355 ± 40.142(54.100)	8553.084 ± 74.793(100.799)	8713.306 ± 101.446(136.721)
Overall	5556.467 ± 68.705(92.595)	6293.873 ± 69.194(93.254)	7377.905 ± 90.828(122.410)	7658.195 ± 81.496(109.833)

Note: Values are Mean Absolute Error (MAE) ± 95% CI half-width (99% CI half-width).

Table 22: Heston Model MAE by Moneyness Bucket - Prices (Short Term)

Maturity	ATM	MID	WINGS	Overall
0.72	13743.968	6933.476	6525.453	7933.055
1.08	5210.286	9198.715	7924.574	8425.033
1.44	5450.603	5455.318	7874.191	8840.983
1.81	10314.769	10182.393	10902.529	10865.652
2.17	3648.833	4898.612	8309.740	9935.171
Overall	7673.692	7333.703	8607.297	9019.979

Table 23: Price MAE Improvement (Heston – RFSV) in bps - (Short Term)

Metric	ATM	MID	WINGS	Overall
Improvement (Δ MAE)	2117.225	1039.830	1229.392	1361.784

Note: A positive value indicates the RFSV MAE is smaller than the Heston MAE.

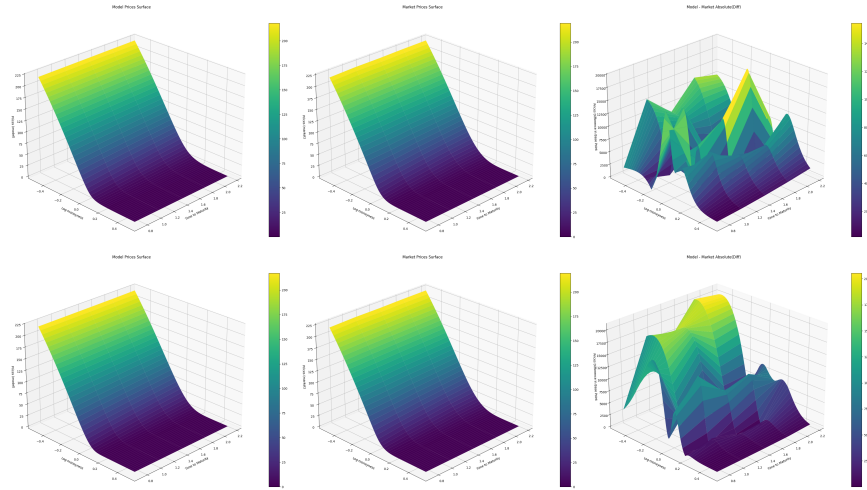


Figure 31: Comparison of the two generated price surfaces with the market, and their errors, on the short-term maturities. RFSV above, Heston below.

13.2 Medium-term.

Table 24: MAE by Moneyness Bucket - Prices (Medium Term)

Maturity	ATM	MID	WINGS	Overall
2.53	2780.056 \pm 32.134(43.307)	7890.455 \pm 97.565(131.489)	3058.860 \pm 27.309(36.804)	4204.283 \pm 46.274(62.364)
2.89	7155.462 \pm 76.095(102.554)	7464.095 \pm 90.921(122.536)	4837.798 \pm 53.186(71.680)	4914.951 \pm 42.979(57.923)
3.25	12777.201 \pm 125.412(169.020)	10158.918 \pm 123.982(167.093)	7170.652 \pm 84.602(114.019)	6749.680 \pm 83.094(111.987)
3.61	20037.934 \pm 219.917(296.386)	16477.792 \pm 187.964(253.322)	10724.271 \pm 138.128(186.157)	10021.295 \pm 113.631(153.142)
Overall	10622.108 \pm 113.950(153.573)	10480.517 \pm 133.155(179.456)	6424.064 \pm 83.080(111.968)	6506.140 \pm 71.547(96.424)

Note: Values are Mean Absolute Error (MAE) \pm 95% CI half-width (99% CI half-width).

Table 25: Heston Model MAE by Moneyness Bucket - Prices (Medium Term)

Maturity	ATM	MID	WINGS	Overall
2.53	1857.603	3759.906	6853.989	6248.929
2.89	3793.156	4473.260	7840.040	7382.907
3.25	7253.523	7114.783	8675.178	8957.284
3.61	12388.054	11466.169	10436.052	11135.827
Overall	6323.084	6703.530	8451.315	8431.237

Table 26: Price MAE Improvement (Heston – RFSV) in bps - (Medium Term)

Metric	ATM	MID	WINGS	Overall
Improvement (Δ MAE)	-4299.024	-3776.987	2027.251	1925.097

Note: A negative value indicates the RFSV MAE is greater than the Heston MAE.

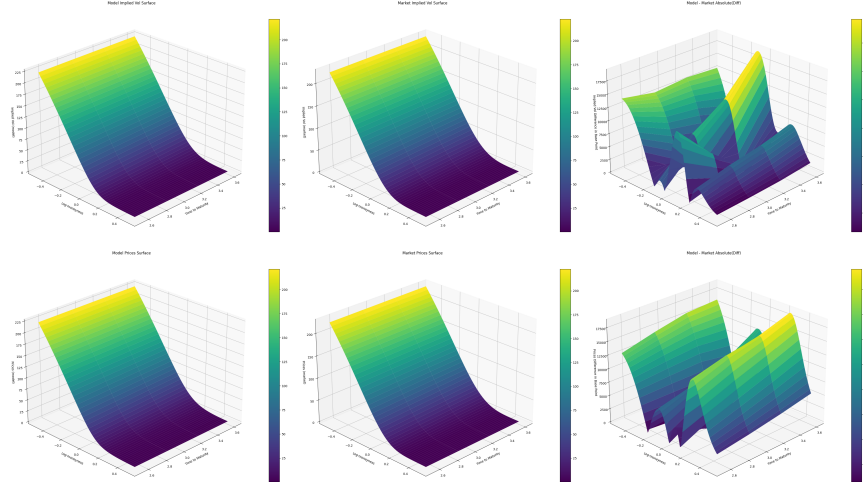


Figure 32: Comparison of the two generated price surfaces with the market, and their errors, on the medium-term maturities. RFSV above, Heston below.

13.3 Out of sample.

Table 27: MAE by Moneyness Bucket - Prices (Out-of-Sample)

Maturity	ATM	MID	WINGS	Overall
3.97	10219.751 \pm 118.127(159.202)	5911.197 \pm 63.413(85.463)	6792.876 \pm 77.487(104.431)	9915.471 \pm 116.986(157.664)
4.69	17673.837 \pm 187.953(253.307)	13060.388 \pm 161.490(217.643)	4930.659 \pm 62.644(84.427)	10550.211 \pm 135.886(183.136)
6.17	34926.411 \pm 342.814(462.016)	30182.692 \pm 367.660(495.501)	14133.621 \pm 126.182(170.057)	18175.970 \pm 235.062(316.797)
Overall	21021.889 \pm 230.716(310.940)	16445.442 \pm 200.705(270.493)	8680.435 \pm 95.432(128.614)	12832.186 \pm 141.235(190.345)

Note: Values are Mean Absolute Error (MAE) \pm 95% CI half-width (99% CI half-width).

Table 28: Heston Model MAE by Moneyness Bucket - Prices (Out-of-Sample)

Maturity	ATM	MID	WINGS	Overall
3.97	18501.514	17079.606	13882.126	14319.060
4.69	26807.718	24470.026	17911.916	18363.659
6.17	44259.186	40916.213	29611.172	28964.530
Overall	29856.139	27488.615	20468.405	20549.083

Table 29: Price MAE Improvement (Heston – RFSV) in bps - (Out-of-Sample)

Metric	ATM	MID	WINGS	Overall
Improvement (Δ MAE)	8834.250	11043.173	11787.970	7716.897

Note: A positive value indicates the RFSV MAE is lower than the Heston MAE. RFSV above, Heston below.

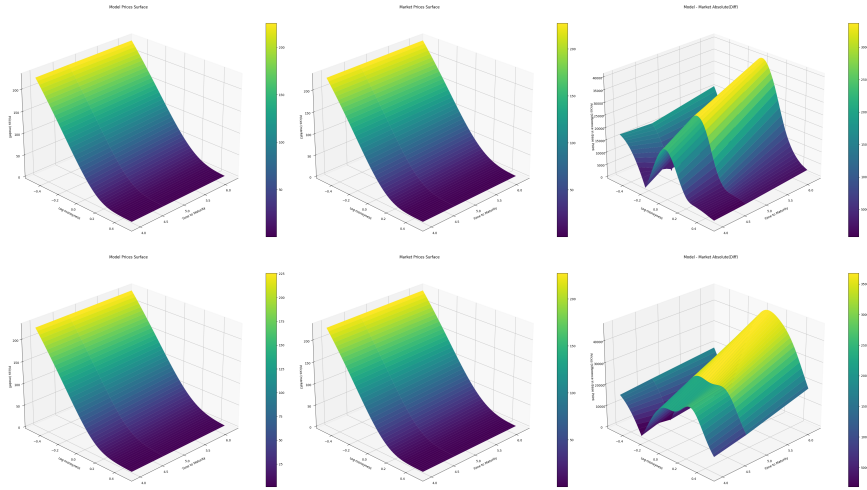


Figure 33: Comparison of the two generated price surfaces with the market, and their errors, on the out-of-sample maturities.

14 Appendix H: Python implementation.

If interested in the full implementation, please refer to the following GitHub repository.



Figure 34: QR code for the GitHub repository

References

- [1] Benoit B. Mandelbrot and John W. Van Ness. “Fractional Brownian Motions, Fractional Noises and Applications”. In: *SIAM Review* 10.4 (1968).
- [2] Ivan Nourdin. *Selected aspects of fractional Brownian motion*. Springer, 2012.
- [3] Lévy P. “Random functions: General theory with special references to Laplacian random functions”. In: *University of California Publications in Statistics* 1 (1953).
- [4] Comte F. and Renault E. “Long memory in continuous-time stochastic volatility models”. In: *Mathematical Finance*, Vol. 8. (1998).
- [5] Cheridito P., Hideyuki K., and Makoto M. “Fractional Ornstein-Uhlenbeck processes”. In: *Electronic Journal of Probability*, Vol. 8. (2003).
- [6] Hull J. and White A. “The Pricing of Options on Assets with Stochastic Volatilities”. In: *The Journal of Finance*, Vol. 42. (1987).
- [7] Scott O. L. “Option Pricing when the Variance Changes Randomly: Theory, Estimation, and an Application”. In: *The Journal of Financial and Quantitative Analysis*, Vol. 22. (1987).
- [8] Melino A. and Turnbull M. S. “The Pricing of Foreign Currency Options”. In: *The Canadian Journal of Economics*, Vol. 24. (1991).
- [9] Heston S. “A closed-form solution for options with stochastic volatility with applications to bond and currency options”. In: *Review of Financial Studies*. Vol. 6. (1993).
- [10] Baillie R., Bollerslev T., and Mikkelsen H. “Fractionally integrated generalized autoregressive conditional heteroskedasticity”. In: *Journal of Econometrics*. Vol. 74. (1996).
- [11] Gatheral J., Jaisson T., and Rosenbaum M. “Volatility is rough”. In: *ArXiv* (2014).
- [12] Comte F. and Renault E. “Long memory continuous time models”. In: *Journal of Econometrics*, Vol. 73. (1996).
- [13] Patrick Billingsley. *Convergence of Probability Measures*. Wiley, 1968.
- [14] Gatheral J. “A parsimonious arbitrage-free implied volatility parameterization with application to the valuation of volatility derivatives”. In: (2004).
- [15] Ferhati T. “SVI model free wings”. In: *arXiv* (2020).
- [16] Gatheral J. and Jacquier A. “Arbitrage-free SVI volatility surfaces”. In: *arXiv* (2024).
- [17] Rogers L. and Tehranchi M. “CAN THE IMPLIED VOLATILITY SURFACE MOVE BY PARALLEL SHIFTS?” In: *Springer* (2008).
- [18] Robert Y. C. and Rosenbaum M. “Volatility and covariation estimation when microstructure noise and trading times are endogenous.” In: *Mathematical Finance* (2012).
- [19] Vollrath I. and Wendland J. “Calibration of Interest Rate and Option Models Using Differential Evolution”. In: *SSRN* (2009).
- [20] Gilli M. and Schumann E. “Calibrating Option Pricing Models with Heuristics”. In: *SSRN* (2010).

- [21] Storn R. and Price K. “Differential Evolution – A Simple and Efficient Heuristic for Global Optimization over Continuous Spaces”. In: *Journal of Global Optimization*, Vol. 11. (1997).
- [22] Schoutens W., Simons E., and Tistaert J. “A Perfect Calibration ! Now What ?” In: *Springer* (2003).
- [23] Kendall Atkinson. *An Introduction to Numerical Analysis*. Wiley, 1989.
- [24] Albrecher H. et al. “The Little Heston Trap”. In: (2006).
- [25] Kahl C. and Jackel P. “Not-so-complex logarithms in the Heston model”. In: *Wilmott Magazine* (2005).